Journal of Neuroinflammation

RESEARCH

Open Access

IFN-γ signaling links ventriculomegaly to choroid plexus and ependyma dysfunction following maternal immune activation

Yu-Qin Sun[1†], Xin-Xin Huang[1,3†], Wei Guo[1], Chen Hong[1], Juan Ji[1], Xi-Yue Zhang[1], Jin Yang[1], Gang Hu[1] and Xiu-Lan Sun[1,2*]

Abstract

Maternal immune activation (MIA) is a principal environmental risk factor contributing to autism spectrum disorder (ASD) and can be causally linked to ASD symptoms. In our study, we found that MIA triggered by poly (I: C) injection caused ventriculomegaly in offspring due to the dysfunction of the choroid plexus (Chp) and ependyma. We subsequently identified a sustained enhancement of interferon-γ (IFN-γ) signaling in the brain and serum of MIA offspring. Further study revealed that increased IFN-γ signaling could disrupt the barrier function of Chp epithelial cells by activating macrophages, and suppress the differentiation of primary ependymal cells via the signal transducer and activator of transcription 1/3 signaling. The effects of MIA on the offspring were mitigated by administration of IFNGR-blocking antibody in pregnant dams, while systemic maternal administration of IFN-γ was sufficient to mimic the effect of MIA. Overall, our findings revealed that ventriculomegaly caused by IFN-γ signaling could be a critical factor in compromising fetal brain development in MIA-induced ASD and provide a mechanistic framework for the association between maternal inflammation and abnormal development of ventricles in the offspring.

Keywords Ventriculomegaly, ASD, MIA, IFN-γ, Choroid plexus, Ependyma

Introduction

Autism spectrum disorder (ASD) represents a complex neurodevelopmental disorder characterized by its core symptoms of social deficiency and repetitive, stereotyped behavioral patterns [1]. Maternal immune system activation (MIA) during embryonic development is a significant risk factor for ASD [2, 3]. MIA triggered by maternal infections leads to a systemic inflammatory response, producing pro-inflammatory cytokines such as interleukin-6 (IL-6) and tumor necrosis factor-α (TNF-α), which could cross the placental barrier and affect the development of the fetal brain and increase the risk of neurodevelopmental disorders in offspring [4, 5]. Clinical studies have also detected elevated levels of inflammatory biomarkers, including cytokines and chemokines in the

†Yu-Qin Sun and Xin-Xin Huang contributed equally to this work.

*Correspondence:
Xiu-Lan Sun
xiulans@njmu.edu.cn
[1]Neuroprotective Drug Discovery Key Laboratory, Jiangsu Key Laboratory of Neurodegeneration, State key laboratory of reproductive medicine and offspring health, Nanjing Medical University, Nanjing, Jiangsu 211166, China
[2]Nanjing University of Chinese Medicine, The Affiliated Hospital of Nanjing University of Chinese Medicine, Nanjing, China
[3]Zhongda Hospital, School of Medicine, Southeast University, Nanjing, China

serum, plasma, and cerebrospinal fluid of ASD patients [6]. However, the pathological mechanisms of transient inflammation-induced neurodevelopmental disorders remain unclear.

Recent studies revealed that MIA triggers an inflammatory state in the choroid plexus (Chp) and abnormal neurogenesis in the subventricular zone (SVZ) of offspring during the embryonic stage [7–9]. The Chp comprises various types of cells and has a highly regulated immune-secretory capacity, producing approximately 80% cerebrospinal fluid (CSF) through a coordinated action of multiple ion and water transport molecules [10, 11]. Ependymal cells (ECs) lining the cerebral ventricles are derived from the SVZ radial glia and fully differentiated by the second week of postnatal life [12]. ECs are covered by motile cilia, whose coordinated beating facilitates the directional flow of CSF [13]. An abnormal function and structure of Chp or ependyma induces CSF circulation failure, leading to ventriculomegaly. Ventriculomegaly is one of the most common brain abnormalities diagnosed prenatally in fetuses. Recent studies have shown that children with ASD exhibit ventricular dilation as early as their developmental stage, with a significant positive correlation between the degree of ventricular enlargement and the severity of behavioral defects [14, 15]. This indicates that the potential association between ventricular enlargement caused by CSF circulation abnormalities and neurodevelopmental disorders warrants further investigations. However, the specific pathological mechanism underlying ventriculomegaly in ASD patients remains unclear, and whether MIA can lead to ventriculomegaly in offspring mice by affecting CSF circulation is still unknown.

In this study, we first found that MIA offspring exhibited ventriculomegaly and further uncovered the dysfunction of the Chp and ependyma. Subsequently, bulk RNA sequencing (RNA-seq) was performed to explore the underlying mechanisms. We found that interferon-γ (IFN-γ) signaling significantly increased in MIA offspring. Mechanically, IFN-γ signaling disrupted the differentiation of ECs and the barrier function of Chp epithelial cells (CHPEs). Strikingly, administration of IFN-γ neutralizing antibody protected against MIA-induced ventriculomegaly and ASD-like behaviors, while systemic maternal administration of IFN-γ was sufficient to mimic the effect of MIA. Therefore, we provide a mechanistic framework for the association between maternal inflammation and abnormal development of ventricles in offspring, which may contribute to the understanding of the etiological mechanisms underlying neuropsychiatric disorders.

Methods and materials

Experimental animals

For the animal experiments, both female and male C57/B6J mice at 1, 3, and 8–12 weeks after birth were utilized, which were from the Medical Experimental Animal Center of Nanjing Medical University. They were provided with sterilized feed and water and placed in an SPF-grade animal facility. The facility maintained a temperature of around 25 °C, humidity ranging from 50 to 60%, and a 12-hour light-dark cycle.

The animal experiments were conducted in strict accordance with the ARRIVE guidelines and had obtained approval from the Experimental Animal Ethics Committee of Nanjing Medical University (approval number: 2004037-1). Throughout the study, every possible measure was taken to minimize both the number of sacrificed mice and any pain or distress they might endure.

Purification and culture of primary ependymal cells

Primary culture of ECs was performed as previously reported [16]. From postnatal day 1–2 (P1-2) Sprague-Dawley (SD) rats, the SVZs were dissected in pre-cooled PBS. Then, they were digested with trypsin (Gibco, 27250018) and DNAse I (Yeasen, 20156ES50) in PBS at 37 °C for 15 min, after which the mixture was centrifuged. The resulting cell pellet was resuspended in DMEM containing 10% FBS and 1% Penicillin/Streptomycin (Gibco, 151400), and the cell suspension was seeded onto a Poly-L-lysine (PLL)-coated (Sigma, P6407) T25 flask. The cells were allowed to proliferate for 5 days until they reached confluence. Subsequently, the flask was shaken at 250 revolutions per minute (rpm) overnight at room temperature to remove non-adherent microglia. The pure, confluent ependymal progenitors were then transferred to PLL-coated cover slides or plates containing DMEM with 10% FBS and 1% P/S and incubated overnight. To initiate the gradual differentiation of ependymal cells in vitro, the culture medium was replaced with serum-free DMEM supplemented with 1% P/S. For subsequent experiments, IFN-γ (Peprotech, 315-05; at a concentration of 50 ng/mL), Fludarabine (MCE, HY-B0069; 10 μM), and Stattic (MCE, HY-13818; 1 μM) were utilized.

Purification and culture of primary choroid plexus epithelial cells (CHPEs)

Purification and culture of primary choroid plexus epithelial cells (CHPEs) were conducted as previously described [17]. The choroid plexus (Chp) was isolated from the lateral ventricles (LVs) of P1-2 Sprague-Dawley (SD) rat brains. It was then placed in fresh Dulbecco's Modified Eagle Medium (DMEM) and digested with a combination of trypsin and DNase I in phosphate - buffered saline (PBS) at 37 °C for 15 min. After digestion, 3–4 volumes of CHPE culture medium, which consisted

of 1% penicillin/streptomycin (P/S), 1% insulin-transferrin-selenium (ITS), 10 ng/mL epidermal growth factor (EGF), and 10% fetal bovine serum (FBS) in DMEM, were added to halt the digestion process. The resulting mixture was gently pipetted and centrifuged at 1000 revolutions per minute (rpm) for 5 min. Subsequently, the cell pellet was resuspended in fresh CHPE culture medium until no visible sediment was present. The cell suspension was then filtered through a 70-μm cell strainer. After filtration, the cells were seeded into well plates that had been pre-coated with poly-L-lysine. In the subsequent experiments, we used IFN-γ at a concentration of 100 ng/mL and Fludarabine at a concentration of 10 μM.

Primary

The tibiae and femurs were obtained from 7-8-week-old male C57BL/6J mice. The bone marrow within them was flushed out with DMEM. Next, the cell suspension was filtered through 70 μm filters. After that, the cells were incubated in 1 ml of erythrocyte-lysing buffer for 5 min to eliminate erythrocytes. Once the incubation was complete, the cells were washed, and then resuspended in a macrophage culture medium. This medium was composed of 1% penicillin/streptomycin (P/S), 10% L929 cell supernatant, and 20% fetal bovine serum (FBS) in DMEM. The resuspended cells were then seeded onto plates and cultured for 6–7 days to allow for differentiation. For the following experiment, IFN-γ (100 ng/mL) and Fludarabine (10 μM) were used.

Migration assay

Macrophages were seeded in 8 μm Transwell chambers and cultured alone until the seventh day. They (in Transwell chambers) were then transferred to a CHPE culture plate for co-culturing with the CHPEs. The culture media in both the upper and lower chambers were replaced with regular complete medium (10%FBS, 1%P/S in DMEM), with or without the addition of IFN-γ. After 24 h of incubation, the Transwell chambers were removed, and the cells were fixed. Crystal violet (Beyotime, C0121) was applied for staining 10 min, followed by 4 rinses with PBS. The cells on the inner layer of the chamber were gently wiped off with a cotton swab, leaving only the cells that had migrated to the outer layer, which were then photographed and counted.

Quantification of CHPE permeability

CHPEs were seeded in 0.8 μm Transwell chambers and cultured alone until a confluent monolayer was formed. Cells were then co-cultured with macrophages or the culture medium was replaced with macrophage-conditioned medium supernatant. After 48 h of incubation, the Transwell chambers were transferred to a new plate, and 2 mg/mL FITC-Dextran in Hanks buffer solution was added to the upper chamber, while the lower chamber was filled with regular Hanks buffer solution. The plates were incubated in a CO2 incubator for 1 h, and then the fluids from both the upper and lower chambers were collected for fluorescence intensity measurement.

Luciferase assay

Plasmids included pLVX-Puro-Flag-Stat1, full-length Foxj1 promoter pGL3-Basic and pRL-TK were transfected into HEK393T cells by using the Lipofectamine™ 3000 Transfection Reagent (Thermo Fisher, L3000015). After 48 h of transfection, cells were then processed according to the manufacturer's instructions and Firefly luciferase activity was detected with Dual-Luciferase Reporter Gene Assay Kit (Yeasen, 11402ES60) and Cytation 5 (Biotek).

Maternal immune activation (MIA) model

MIA model was conducted as widely reported [18]. Adult (postnatal 8–12 weeks) male mice were mated overnight with females. Females were checked for vaginal plugs the following day, with positive plugs indicating Embryonic Day 0.5 (E0.5). On E12.5, pregnant mice were intraperitoneally injected with poly(I: C) (Sigma Aldrich, P9582; 20 mg/kg) or PBS. All pups remained with the mother until weaning on P21, at which time mice were group-housed at a maximum of 5 per cage with same-sex littermates. Behavioral tests were conducted in adulthood, with at least one-week interval between each test. Anti-Ifngr (Bio-X-cell, BE0029) or IgG (Bio-X-cell, MOPC-21) were administered to pregnant mice at a dose of 500 μg per mouse via intraperitoneal injection 6 h before poly(I: C) or PBS injection on E12.5; IFN-γ was administered at a dose of 5000 U per mouse via intraperitoneal injection on E12.5, with PBS serving as the control vehicle at an equivalent dose.

Three-chamber social approach assay

The social behavior of adult offspring was assessed using a three-chamber social approach test [19]. Initially, the mice were individually housed in clean cages for 1 h to get habituated. Subsequently, they were introduced into a three-chamber arena that had cages with empty objects. The acclimation process lasted for 10 min, divided into two 5-minute sessions spread over a period of 3–4 h. On the next day, the mice were placed in the center chamber, with access to the left and right social test areas blocked. They were allowed to explore the center area for 5 min. After this exploration phase, the barriers separating the adjacent chambers were removed. One of the left and right arenas housed a social object (an unfamiliar C57BL/6 male mouse), while the other contained an inanimate object (a plastic toy). The experimental mice were given 10 min to explore both chambers. The

approach behavior was measured in terms of the interaction time (such as sniffing and approaching) with the targets in each chamber. Only interactions within 2 cm were counted, excluding non-nose contact or exploration.

Videos were recorded during the experiment and analyzed using the ANY-maze system to determine the object exploration time and the total distance the mice moved. A social preference index represented the proportion of time spent investigating the social target relative to the total exploration time of both objects.

Self-grooming assay

Self-grooming assay was performed as previously described [20]. Adult offspring were introduced into a glass beaker (6.5 cm in diameter and 12 cm in height) and allowed to acclimate for 10 min. Following this habituation period, self-grooming behavior was video-recorded for an additional 10 min. Investigators then observed the recordings and quantified the time spent grooming the fur.

Marble burying assay

Marble burying assay was performed as previously described [21]. Adult offspring were acclimated for 0.5–1 h in separate clean holding cages. Then mice were placed in a box measuring 40 × 20 × 30 cm, with a bedding depth of 3 cm, and 20 marbles (arranged in 4 rows and 5 columns) were placed on the bedding. After 15 min of exploration, the mouse was removed, and the degree of marble burying was observed and recorded. The burying index (extent of bedding covering the marbles) was scored as follows: 1 for > 50%, 0.5 for ~ 50%, and 0 for < 50%.

Magnetic resonance imaging (MRI)

During the scanning process using a Biospec 7T/20 USR MRI scanner (Bruker, Germany) at Nanjing Medical University, offspring mice were anesthetized with 5% isoflurane in a nitrogen-oxygen mixture (70%: 30%). The mice were positioned in a prone position on the small animal MRI scanning bed. After their heads were immobilized, T2-weighted imaging was carried out. The imaging parameters for the scan were configured as follows: the repetition time (TR) was set at 3000 milliseconds, the echo time (TE) was 33 milliseconds, the field of view (FOV) measured 3.5 cm by 3.13 cm, and the in-plane matrix size was 256 × 256 pixels. A total of 25 slices were acquired, with each slice having a thickness of 0.7 mm.

Ventricular dye injections

Anesthetized mice were secured horizontally on a stereotactic apparatus, the skull and fontanel were exposed, and a hole was drilled for right lateral ventricle positioning (AP, -0.1 mm; ML, 0.85 mm). Using a microinjector inserted 1–2 mm, 10 μL of Evans blue (EB, Solarbio, E8010), which was dissolved at a concentration of 0.5% in sterile phosphate-buffered saline (PBS), was slowly and uniformly injected. Mice were perfused with PBS after 1 h, followed by brain removal and sectioning for EB outflow observation.

CSF production rates measurements

CSF production rates were measured according to published protocols [22]. Briefly, mice were put under anesthesia, and a hole was drilled for right lateral ventricle positioning as previously described. A PE-10 tube, sealed at the end, was inserted 1–2 mm and fixed with dental cement. Subsequently, the mice were placed vertically with their heads downward at a 90° angle to their bodies. The cisterna magna was exposed, and a PE-10 tube filled with mineral oil (Sigma, M5310) and connected to a 30 G needle was inserted 2 mm and secured with glue and dental cement to block the aqueduct. One microliter of mineral oil was infused at a rate of 1 mL/min for 1 min, and then the sealed tip of the cannula exiting the right ventricle was cut to enable the outflow of CSF. The cerebrospinal fluid outflow conditions of the offspring mice were uniformly recorded over a one-hour period, with measurements taken every 10 min. The volume of CSF was calculated using the formula: CSF volume = $\pi \times \text{Radius}^2 \times \text{length}$.

Quantification of Blood-CSF barrier (B-CSFB) permeability

FITC-Dextran (Beyotime, ST2930) was dissolved in sterile PBS and administered to mice via tail vein injection at a dose of 75 mg/kg. One hour later, 2 μL of mouse CSF is collected from the cisterna magna, diluted in 100 μL PBS, and the fluorescence intensity of the liquid is measured.

CSF flow measurements

We used a vibratome to section a fixed region (spanning Bregma − 0.2 to 0.8 mm) of freshly dissected mouse brains at a thickness of 1 mm, and placed in DMEM containing 0.2% polystyrene beads (Sigma Aldrich, L1030). We recorded the movement of fluorescent beads using LSM710, and captured images from 2 fixed positions at different planes within both the left and right lateral ventricles of each section. A total of 60 frames (10 s) were employed to track the trajectories of bead movements and the speed of individual beads was measured using the 'TrackMate' plugin for Fiji [23].

Quantification of lymphatic drainage

As described in a previous study [24], the cervical fur of the mice was removed to reduce the loss of fluorescence signals. Mice were then treated in two ways. Firstly, 5 μl of OVA-647 (Invitrogen, O34784, with a concentration of 2 mg/ml in PBS) was injected into the cisterna magna

of the mice at a rate of 1 μl/min. Secondly, some mice received an intranasal administration of 5 μl of OVA-647 (2 mg/ml in PBS).

The IVIS Lumina Series III system was employed to measure the fluorescence intensity at different time points (15, 30, and 60 min) after the injection. The results were analyzed using Living Image 4.7.3 (PerkinElmer). To ensure accurate measurements, the background fluorescence was normalized by using naive mice as controls.

Paraffin section staining

After the mice were anesthetized, they underwent transcardial perfusion. First, 37 °C saline was perfused, followed by 4% paraformaldehyde (PFA). After that, the brains were carefully removed and placed in 4% PFA for post-fixation at 4 °C for 24 h. Subsequently, the brains were embedded in paraffin. Coronal sections were cut at an interval of 4 mm. These coronal sections then went through a series of processing steps. They were first placed at 60 °C for 60 min to melt the paraffin, after which they were deparaffinized and rehydrated. For hematoxylin and eosin (H&E) staining, the HE staining kit from Servicebio (G1076) was utilized.

For immunofluorescence (IF), 0.01 mol/L citric acid solution was used for microwave high-temperature repair for 15 min and allowed to cool to room temperature. Blocking solution (containing 10% goat serum and 0.1% Triton X-100) was added and incubated at room temperature for 1 h. The primary antibodies included Foxj1 (Thermo Fisher, 14-9965-82), Sox2 (Cell signaling technology, #23064), Ace. Tub (Sigma, T7451), occludin (Proteintech, 27260-1-AP), Iba1 (WAKO, 019-19741), β-Catenin (Proteintech, 66397-1-Ig), IFNGR1 (Thermo Fisher, MA5-35147), pNKCC1 (Sigma, ABS1004) are applied and incubated at 4 °C overnight. The next day, sections were taken out and warmed up for 1 h, washed with PBS four times, each for 5 min, then the fluorescent secondary antibody included Alexa Fluor- 488-conjugated donkey anti-rabbit (Invitrogen, A-21206), Alexa Fluor-555-conjugated donkey anti-mouse (Invitrogen, A-31570), Alexa Fluor-555-conjugated donkey anti-rabbit (Invitrogen, A31572), and Alexa Fluor-488-conjugated donkey anti-mouse (Invitrogen, A-21202), was applied and incubated at room temperature in the dark for 1 h. After washing, the sections were mounted with Mounting Medium with DAPI (Abcam, ab104139).

For immunohistochemistry (IHC), after rehydration, 3% hydrogen peroxide PBS solution was used to inactivate peroxidase, followed by microwave high-temperature repair with citric acid as in the IF steps. After cooling to room temperature, the sections are blocked and incubated with the primary antibody IFNGR1 (Thermo Fisher, MA5-35147) overnight. The next day, the sections are washed and incubated with the secondary antibody (Bioworld, BS22356), followed by further washing. After the final wash, the DAB chromogen solution (KeyGEN, KGB4101) was used for the colorimetric reaction. The reaction was terminated by adding PBS, followed by hematoxylin counterstaining for a few seconds, and then gradient dehydration and sealing with neutral resin.

For each mouse, three sections were selected, and at least two microscopic fields per section were analyzed using a laser-scanning confocal fluorescence microscope (LSM710). The average of these data was then taken.

Cell IF

Cells were seeded on the pre-coated culture slides. They were fixed with 4% PFA (for ECs and macrophages) or pre-cooled methanol (for CHPEs) at -20 °C for 15 min, followed by three 5-minute washes with PBS. A blocking solution (10% donkey serum in PBS) was applied for 1 h. The primary antibodies included Foxj1 (Thermo Fisher, 14-9965-82), Ace. Tub (Sigma, T7451), Occludin (Proteintech, 27260-1-AP), β-Catenin (Proteintech, 66397-1-Ig), and CD68 (Biolegend, 137001) was added and incubated overnight at 4 °C. On the following day, cells were washed with PBS. After incubation with the fluorescent secondary antibody in the dark, further washes were conducted. The slides with cells were then carefully removed from the well plate and mounted onto glass slides with Mounting Medium with DAPI.

Quantitative polymerase chain reaction (qPCR)

We performed total RNA extraction by RNAiso Plus (Takara, 9108), followed by chloroform extraction, isopropanol precipitation, washing with absolute ethanol, and dissolution. Subsequently, the RNA concentration and purity were determined. Based on the concentration, the volume containing 1000 ng of RNA was calculated. The TAKARA reverse transcription system was then used by adding 2 μL of reverse transcription Mix (ABM, G490) and supplementing with DEPC water to a total volume of 20 μL. Reverse transcription was performed under the following conditions: 37 °C for 15 min, 87 °C for 5 s, followed by holding at 4 °C. The resulting cDNA was subjected to subsequent qPCR analysis on QuantStudio 5 (Thermo Fisher). The amplification reaction mixture consisted of 10 μL, including 1 μL of cDNA, 1 μL of each forward and reverse primer, 5 μL of SYBR Green PCR Master Mix (Selleck, B21202), and DEPC water added to make up the final volume to 10 μL. We conduct analysis on the acquired qPCR data employing the ΔΔCt method in conjunction with normalization procedures. Sequences of all primers are listed in Supplementary Table 1.

Scanning electron microscopy (SEM)

The whole lateral wall of the LV was immersed in freshly made 2.5% glutaraldehyde solution and left to fix overnight at a temperature of 4 °C. After that, it underwent dehydration in a series of gradient ethanol solutions. Subsequently, the sample was dried using the Tousimis Sandai 790 (manufactured by Tousimis Research Corp). Following this, palladium coating was applied to the sample in an IB-5 ion coater. Finally, the coated sample was imaged by a scanning electron microscope (JEOL, model JSM- 900 F).

Western blot (WB)

Tissues and cells were homogenized in RIPA buffer (KeyGEN, KGB5203) with proteinase inhibitor (Roche, 04693132001) and phosphatase Inhibitor (Roche, 04906837001) to generate lysates, which were centrifuged at 4 °C, 12,000 g for 20 min. Protein concentrations were measured using a BCA Protein Assay Kit (KeyGEN, KGB2101). Protein lysates were boiled at 95 °C for 10 min. Equal amounts of lysates (15 mg) were loaded into a polyacrylamide gel and electrophoresis was performed. We then transferred the samples to PVDF membranes at 4 °C for 2 h, and blocked the membranes in 5% BSA in TBST at room temperature for 1 h. Then the membrane was incubated at 4 °C overnight with primary antibodies including Foxj1 (Thermo Fisher, 14-9965-82), Actin (Proteintech, 66009-1-Ig), Stat1 (Protrintech, 10144-2-AP), pStat1 (Affinity, AF3300), Stat3 (Santa Cruz, sc-8019), pStat3 (Santa Cruz, sc-81523), β-catenin (Proteintech, 66397-1-Ig), occludin (Proteintech, 27260-1-AP), Icam1 (Santa Cruz, sc-18853). After being washed in TBST 3 times, the incubation of the membranes was completed by adding HRP-conjugated anti-mouse antibody (Proteintech, SA00001-1) or HRP-conjugated anti-rabbit antibody (Proteintech, SA00001-2) for 1 h at room temperature. Once the washing process was thoroughly completed, signals were detected by the ECL developing solution (Vazyme, E433-01) and imaged using an automatic chemiluminescence image analysis system (5200, Tanon) digital image scanner. Quantification of individual protein bands was performed by densitometry using ImageJ software.

Enzyme-linked immunosorbent assay (ELISA)

After enucleating the offspring to collect blood, let the whole blood stand at room temperature for 1 h, then centrifuge at 1000 rpm for 15 min. Collect the supernatant, mix it well, and use it for ELISA detection. Follow the kit (Cloud-Clone Corp, SCA049Mu) instructions to complete the preparation of standards and test solutions, add samples, wash the plate, substrate reaction, and measure the absorbance.

RNA-seq Preparation and sequencing

Total RNA was extracted using RNAiso Plus, and RNA quality was assessed with an Agilent 2100 Bioanalyzer (Agilent Technologies). RNA-seq libraries were prepared with the NEBNext Ultra RNA Library Prep Kit for Illumina (NEB, 7530), and sequencing was conducted on the Illumina NovaSeq 6000 platform with paired-end reads. Raw reads were quality-filtered and adapters were removed using fastp (version 0.18.0). Paired-end clean reads were aligned to the mouse reference genome Ensembl_release106 using HISAT2 (version 2.4). Gene-level quantification and normalization were carried out with RSEM (version 1.3.3), and gene expression was measured as fragments per kilobase of transcript per million mapped reads (FPKM). For identifying differentially expressed genes (DEGs), a significance threshold was established. Specifically, genes with a P-value less than 0.05 and a fold-change greater than 1.5 or less than 0.6667 were considered significant. Subsequently, KEGG and GO enrichment analysis were performed on DEGs to identify the regulation of biological processes. GSEA was performed with clusterprofile R packages (4.12.0) using signatures from the hallmark Molecular Signatures Database (MSigDB).

Quantification and statistical analysis

Statistical analysis was carried out on data from groups where $n \geq 3$. Here, "n" represents the number of subjects in in-vivo experiments and the number of replicates in in-vitro ones. The data were processed using GraphPad Prism 9.0 software. The Shapiro-Wilk test was employed to check for normality, and the Brown-Forsythe test was used to assess variance homogeneity. When comparing two groups, different tests were applied according to the data characteristics. An Unpaired T test (or a corrected T test for cases of unequal variances) was used for normally distributed data. For multi-group comparisons, different methods were also selected based on the data properties. One-way or Two-way ANOVA (combined with Sidak's multiple comparisons test or Dunnett's multiple comparisons test) was used for data that were normally distributed and had homogeneous variances. Non-parametric tests were applied when the data did not follow a normal distribution. The significance level was set at $P < 0.05$. The data are presented in the form of MEAN ± SEM.

Results

MIA offspring exhibited a phenotype of ventriculomegaly

First, we investigated whether ventriculomegaly, observed in ASD patients, also existed in mouse models of MIA. Pregnant dams were injected intraperitoneally with poly (I: C) or vehicle (PBS) on embryonic day (E) 12.5. Subsequent behavioral testing of the adult (postnatal 8–12 weeks) offspring confirmed the presence of

ASD-like behaviors; specifically, decreased social indices (social defects), increased marble-burying indices (repetitive and stereotypical behaviors), and prolonged grooming durations (anxiety-like behaviors; Fig. 1a–c).

Using magnetic resonance imaging (MRI) and coronal brain sections stained with hematoxylin and eosin (H&E), we observed a significant dilation of the lateral ventricles (LVs) in adult MIA male offspring but not in female offspring (Fig. 1d–g), suggesting that MIA led to sex-specific ventriculomegaly in offspring. Consequently, our subsequent experiments were solely conducted on the adult male offspring, unless otherwise noted. Furthermore, we uncovered a significant positive correlation between the degree of ventriculomegaly and the severity of various ASD-like behaviors in the offspring via correlation analysis (Fig. 1h-j), implying a potential link between the neurobehavioral abnormalities and ventriculomegaly in MIA offspring.

We monitored the ventricle size of offspring in postnatal one week (1w) and three weeks (3w) to further investigate the developmental changes in the LVs of MIA offspring. Given the limitations of performing

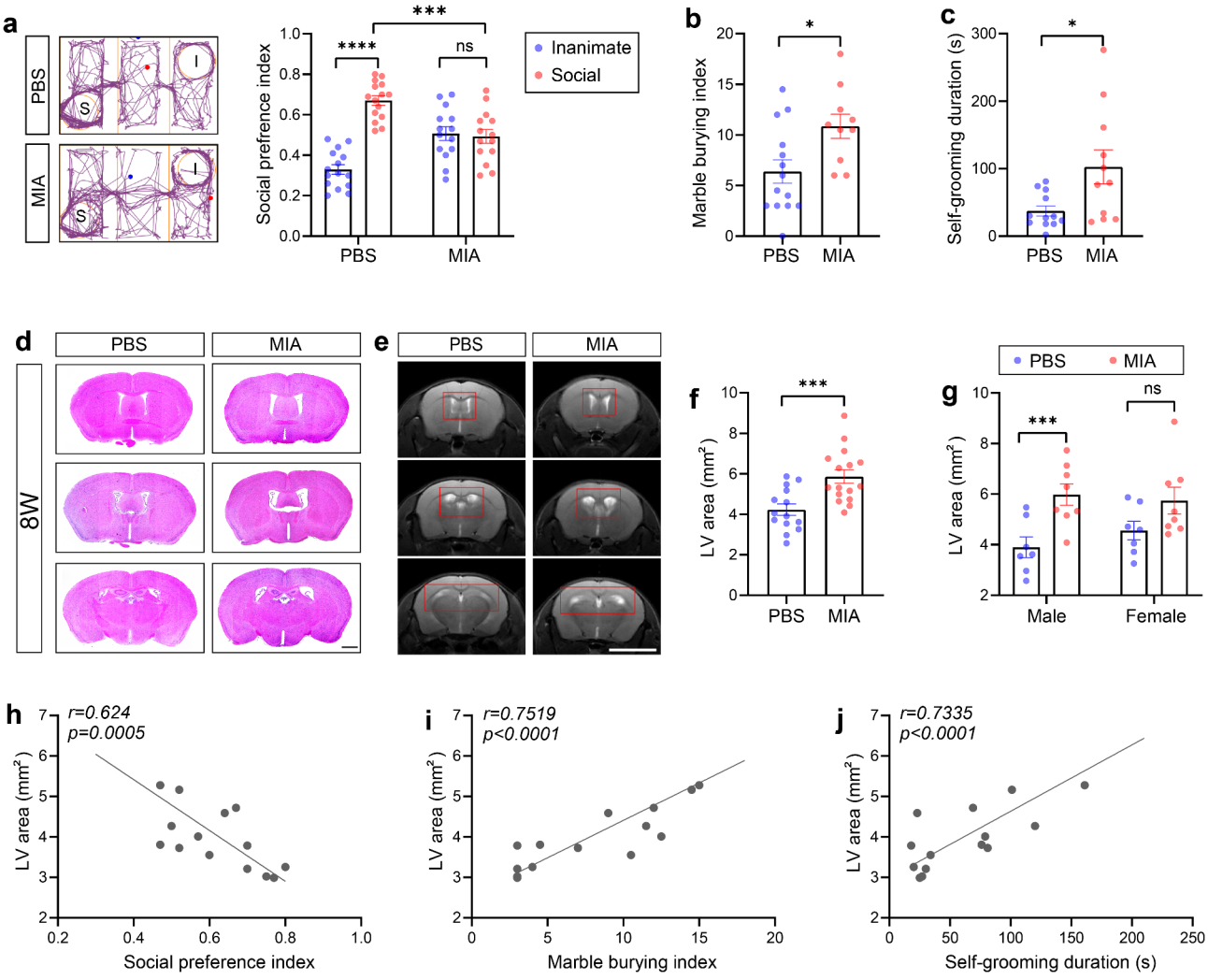

Fig. 1 MIA triggers ventriculomegaly in male offspring. (**a**) The three-chamber social preference test was used to assess the social preference of the offspring, where the Social preference index represents the proportion of time spent by the mouse in social interaction with a social target relative to the total duration of the test ($n = 14–15$ from 4–5 litters). Two-way ANOVA tests were applied. *** $P < 0.001$ and **** $P < 0.0001$. (**b**) The marble burying test was used to assess anxiety behavior in the offspring ($n = 10–14$ from 4–5 litters). Unpaired T tests were applied. * $P < 0.05$. (**c**) The grooming test was used to assess repetitive grooming behavior in the offspring ($n = 10–14$ from 4–5 litters). Unpaired T tests were applied. * $P < 0.05$. (**d**) Representative H&E staining of brain sections from adult offspring corresponding to the position shown in (**e**). Scale bar, 1 mm. (**e**) Representative MRI images of brain in offspring, with the LVs indicated within the red squares. Scale bar, 5 mm. (**f**) MRI measurement of LVs areas in adult offspring, with the statistical method referring to the methodology in the first section: five consecutive scans starting 0.4 mm posterior to the anterior fontanelle (towards the cerebellum) were used to measure the ventricle area, which was then summed and statistically analyzed ($n = 14–16$ from 4–5 litters). Unpaired T tests were applied. *** $P < 0.001$. (**g**) MRI results of CSF volume in adult offspring, stratified by sex ($n = 7–8$ from 4–5 litters). Two-way ANOVA tests were applied. ** $P < 0.01$. (**h**-**j**) Correlation analysis results between the social preference index, marble burying index, and grooming duration of the offspring and the LVs area ($n = 13$ from 4–5 litters)

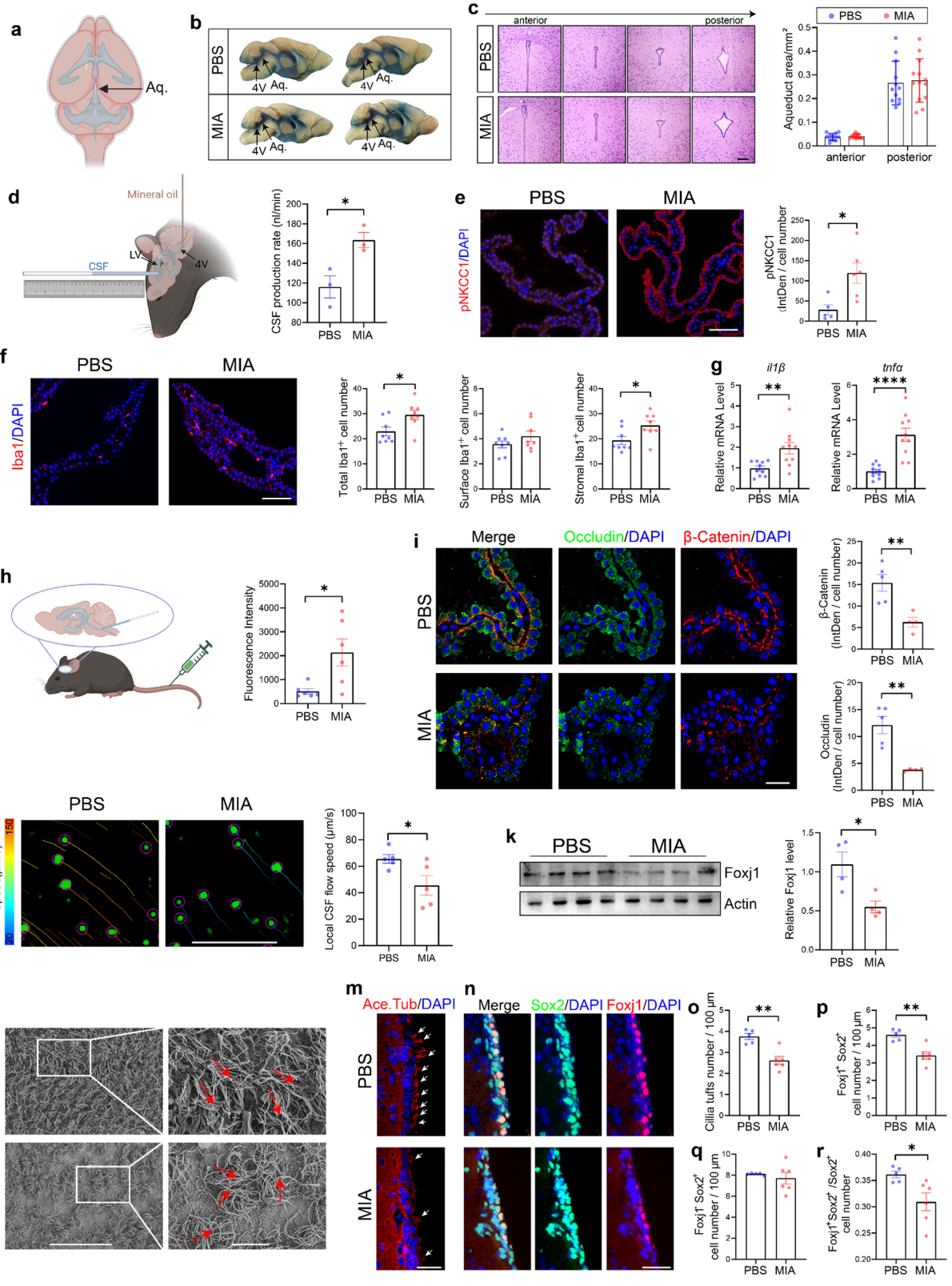

Fig. 2 (See legend on next page.)

(See figure on previous page.)

Fig. 2 Structural and functional abnormalities of the Chp and ependyma in MIA offspring. (**a**) Schematic diagram of the cerebral aqueduct location within the brain. (**b**) Representative images of brain slices after Evans Blue detection of CSF outflow, with arrows indicating the cerebral aqueduct (Aq) and the fourth ventricle (4 V). (**c**) Representative H&E staining of brain slices from the anterior to the posterior cerebral aqueduct in offspring. Scale bar, 100 μm. Quantification of the anterior and posterior areas of the cerebral aqueduct ($n = 12$–13 from 4–5 litters). Two-way ANOVA tests were applied. (**d**) Schematic diagram of the method for detecting the rate of CSF production in offspring and quantification of CSF production rate ($n = 3$ from 3 litters). Unpaired T tests were applied. * $P < 0.05$. (**e**) Representative IF staining of pNKCC1 in the Chp of offspring and quantification of fluorescence intensity ($n = 5$–6 from 3 litters). Scale bar, 100 μm. Unpaired T tests were applied. * $P < 0.05$. (**f**) Representative IF staining of Iba1$^+$ macrophages in the Chps of offspring, and quantification of macrophage infiltration in the total (left), apical (middle), and stromal (right) regions of the Chps ($n = 8$ from 3–4 litters). Scale bar, 100 μm. Unpaired T tests were applied. * $P < 0.05$. (**g**) qPCR analysis of il1β and tnfα mRNA levels in the Chp of offspring ($n = 10$ from 3–4 litters). Unpaired T tests were applied. ** $P < 0.01$ and **** $P < 0.0001$. (**h**) Schematic diagram of the method for detecting blood-CSF barrier leakage using FITC-dextran and the quantification of fluorescence intensity in the CSF of offspring ($n = 6$ from 3–4 litters). Unpaired T tests were applied. * $P < 0.05$. (i) Representative IF staining images and quantification of Occludin and β-Catenin fluorescence intensity in the Chp of offspring ($n = 4$–5 from 3 litters). Scale bar, 100 μm. Unpaired T tests were applied. ** $P < 0.01$. (**j**) Representative images of the movement trajectory of fluorescent microspheres in the LVs of offspring and quantification of the movement speed of fluorescent microspheres, each value represents the average movement speed of fluorescent microspheres in 4 fields of view in the brain sections of each mouse. ($n = 5$ from 3 litters). Scale bar, 100 μm. Unpaired T tests were applied. * $P < 0.05$. (**k**) Representative immunoblot images and quantification of Foxj1 protein level in the samples obtained from ependyma of adult offspring ($n = 4$ from 3 litters). Unpaired T tests were applied. * $P < 0.05$. (**l**) Representative SEM images of ependymal cilia in the LVs of offspring, with red arrows indicating the direction of ciliary tufts. Scale bar, 50 μm (low magnification), and 10 μm (high magnification). (**m** and **o**) Representative IF staining images (**m**) and quantification (**o**) of ciliary tufts in the LVs of offspring ($n = 5$–6 from 3–4 litters). Scale bar, 100 μm. Unpaired T tests were applied. ** $P < 0.01$. (**n**-**r**) Representative IF staining images of ECs in the lateral ventricles of offspring (**n**). Scale bar, 100 μm. Quantification of the density of Foxj1$^+$Sox2$^+$ ECs (**p**) and Foxj1$^-$Sox2$^+$ neural progenitor cells (**q**) and the ratio of the two (**r**) ($n = 5$–6 from 3–4 litters). Unpaired T tests were applied. ** $P < 0.01$ and * $P < 0.05$

anesthetized brain MRI on offspring before postnatal 1w, we directly harvested brains from 1w offspring for H&E staining observation. These results indicated that 1w and 3w MIA offspring exhibited ventriculomegaly (Figs. S1a, b), suggesting that the ventriculomegaly persists from birth through adulthood, with no subsequent compensatory repair processes.

MIA triggered abnormal structure and function in Chp and ependyma of offspring

Ventriculomegaly can be attributed to various factors, such as an overproduction of CSF, dysfunction of ependymal cilia, or a reduction in the reabsorption of CSF [25–27]. A narrowing of the aqueduct of Sylvius, called aqueductal stenosis, is often the most prevalent underlying cause associated with the abnormal buildup of CSF, called hydrocephalus [28]. To determine whether the ventriculomegaly in adult MIA offspring is caused by the blockage of the ventricular system, we carried out histological analysis and investigated CSF outflow through the utilization of the CSF tracer, Evans blue. The results revealed no obstruction in the ventricular channel and no malformation of the central aqueduct in the brains of adult MIA offspring (Fig. 2a–c).

Inflammation of Chp is sufficient to cause nonobstructive hydrocephalus [29, 30]. Subsequently, we measured the production rate of CSF by Chp in the LV. Our findings confirmed that, in adulthood, the offspring exposed to MIA had a higher rate of CSF production than those from the PBS-treated group (Fig. 2d). Previous studies indicated that inflammatory mediators enhanced the phosphorylation levels of NKCC1, a Na-K-Cl cotransporter expressed on the apical membranes of CHPEs, leading to increased CSF production by the CHPEs [11, 29]. As expected, adult MIA offspring presented with elevated apical membrane expression of phosphorylated NKCC1 (pNKCC1) in Chp and macrophage accumulation within the Chp stromal space (Fig. 2e, f). Moreover, it was also observed that the mRNA levels of IL-1β and tumor necrosis factor-α (TNF-α) were elevated in the Chp of the offspring exposed to MIA (Fig. 2g), suggesting MIA triggered inflammation in Chp of adult offspring.

Inflammatory processes within Chp are recognized to compromise the integrity of the blood-CSF barrier (B-CSFB) [31]. Such perturbations can facilitate the leakage of macromolecules from the bloodstream into CSF, consequently elevating the viscosity y and osmotic pressure of the CSF. These changes may enhance CSF production and hinder its circulation [31, 32]. Thus, to examine B-CSFB of Chp in adult offspring, we intravenously injected the fluorescent dye fluorescein isothiocyanate (FITC-) Dextran and found the level of leakage increased in CSF of adult MIA offspring (Fig. 2h). Similarly, the distribution of occludin and β-catenin in the CHPE of MIA offspring was disrupted; specifically, in Chp of PBS offspring, occludin and β-catenin consistently localized along each cell, whereas the staining patterns in Chp of MIA offspring were disrupted, appearing diffuse (Fig. 2i). Collectively, these data demonstrated that MIA triggered a sustained inflammation and disrupted the B-CSFB in Chp of adult offspring.

Previous studies have reported that ciliary dysfunction in ECs, which are pivotal for CSF flow, can result in hydrocephalus [33–35]. Therefore, next we investigated the impact of MIA on the ependymal function and morphology in adult offspring. Initially, we tracked the movement of the fluorescent microsphere over freshly dissected brain slices containing the LVs to visualize ependymal cilia-generated CSF flow. We observed that the MIA offspring showed slower bead movement than

the PBS offspring, indicating a weakened CSF flow in LVs of adult MIA offspring. (Fig. 2j, Fig. S2).

Subsequently, the ciliary defects in adult MIA offspring were identified by scanning electron microscopy (SEM). Specifically, ependyma of adult MIA offspring exhibited cilia with disrupted orientation, indicating a loss of directional coherence, and a decreased number of cilia (Fig. 2l). The result of cilia staining with acetylated tubulin (Ace. Tub) in LV wall corroborated SEM findings (Fig. 2m, o). In brain slices costained for Foxj1 (a differential transcription factor of ECs) and Sox2 (a marker of neural progenitor cells), we observed a significantly decreased density of Foxj1 + Sox2 + ECs lining the LV wall in adult MIA offspring. There was no significant change in the density of Foxj1-Sox2 + progenitor cells (Fig. 2n, p–r), suggesting that the SVZ precursor cells in MIA offspring underwent abnormal differentiation fate during early development. Further, we examined a lower protein level of Foxj1 expression in the LV wall of adult MIA offspring (Fig. 2k). These results indicated that maternal inflammation impaired the normal CSF flow and the differentiation of ECs in offspring.

In recent years, meningeal lymphatic vessels (mLVs) have been identified as additional routes for CSF drainage to cervical and mandibular lymph nodes [36]. We administered the fluorescent protein OVA647 into the cisterna magna of adult offspring and evaluated CSF drainage efficiency by quantifying fluorescence in their deep cervical lymph nodes. Our findings revealed a significant reduction in lymphatic drainage in adult MIA offspring (Fig. S3a). Additionally, we performed immunofluorescence (IF) staining for the lymphatic endothelial cell marker LYVE-1, which is primarily involved in the absorption and transport of lymphatic fluid [37]. We found that the expression of LYVE-1 in the mLVs of adult MIA offspring significantly decreased (Fig. S3b). These findings suggested that adult MIA offspring exhibited diminished lymphatic drainage, potentially due to reduced functional protein expression within their lymphatic vessels. However, it remains unknown whether mLV dysfunction can directly cause ventriculomegaly in MIA offspring.

Overall, our findings have primarily attributed ventriculomegaly in adult MIA offspring to weakened CSF flow and increased CSF production. Consequently, the following research will primarily focus on the structure and function of Chp and ependyma.

IFN-γ signaling was enhanced in the brain and serum of MIA offspring

The Chp is not only the production center of CSF but also an important bridge between peripheral immunity and the central nervous system (CNS), regulating the health of CNS and immune system through complex mechanisms [38]. We first employed bulk RNA-seq to characterize the transcriptional alterations in Chp of adult PBS and MIA offspring. Differential expression analyses revealed significant differences between MIA and PBS offspring (Fig. 3a, Fig. S4). Consistent with the neuronal developmental abnormalities noted in MIA offspring, our results indicated that the downregulated DEGs within the Chp were enriched in Gene Ontology (GO) terms related to synapse regulation (Fig. 3b). This finding was particularly relevant to the regulation of neurodevelopment in Chp, as reported in previous studies [39, 40]. In addition, we observed a downregulation of genes associated with intercellular junction function in Chp of MIA offspring (Fig. 3b), which aligns with our earlier findings of B-CSFB disruption in these offspring.

Moreover, upregulated DEGs in Chp of MIA offspring were highly enriched for the GO terms related to antivirus and IFN signaling (Fig. 3b). To further validate the robustness of our findings regarding IFN signaling dysregulation, we have performed an independent pathway enrichment analysis using Gene Set Enrichment Analysis and found IFN-β and IFN-γ pathway scores were significantly elevated in MlA offspring compared to PBS offspring (Fig. 3c). The balance between type I and II IFNs is pivotal for the recruitment of immune cells to CNS through Chp [40]. We examined the expression of type I and II IFN-dependent genes in Chp of adult offspring using real-time quantitative PCR. We found that some type I IFN-dependent genes in Chp of MIA offspring, such as interferon regulatory factor 9 (Irf9) and interferon-induced protein with tetratricopeptide repeats 1 (Ifit1), showed increased expression, while others, including IFN-β and interferon regulatory factor 7 (Irf7), remained unchanged. Notably, the expression of type II IFN-dependent genes in Chp of MIA offspring was significantly increased (Fig. 3d), including IFN-γ, C-X-C motif chemokine ligand 10 (Cxcl10), chemokine (C-C motif) ligand 17 (Ccl17), intercellular adhesion molecule 1 (Icam1), and interferon-induced protein with tetratricopeptide repeats 3 (Ifit3). Thus, the IFN-γ signaling was significantly enhanced in Chp of adult MIA offspring.

Additionally, we utilized an enzyme-linked immunosorbent assay (ELISA) to confirm elevated levels of IFN-γ in the serum of adult MIA offspring (Fig. 3e). Correlation analysis further revealed a positive association between serum IFN-γ levels and the size of LV in adult MIA offspring (Fig. 3f). Interferon-γ receptor1 (IFNGR1) immunostaining revealed a significant upregulation of IFNGR1 in both ependyma and Chp of neonatal (postnatal one day) MIA offspring (Fig. 3d). In adults, however, only Chp showed increased IFNGR1 expression, with ependyma expression resembling PBS offspring (Fig. 3h).

Taken together, our data suggested that IFN-γ signaling played a crucial role in the induction of inflammation.

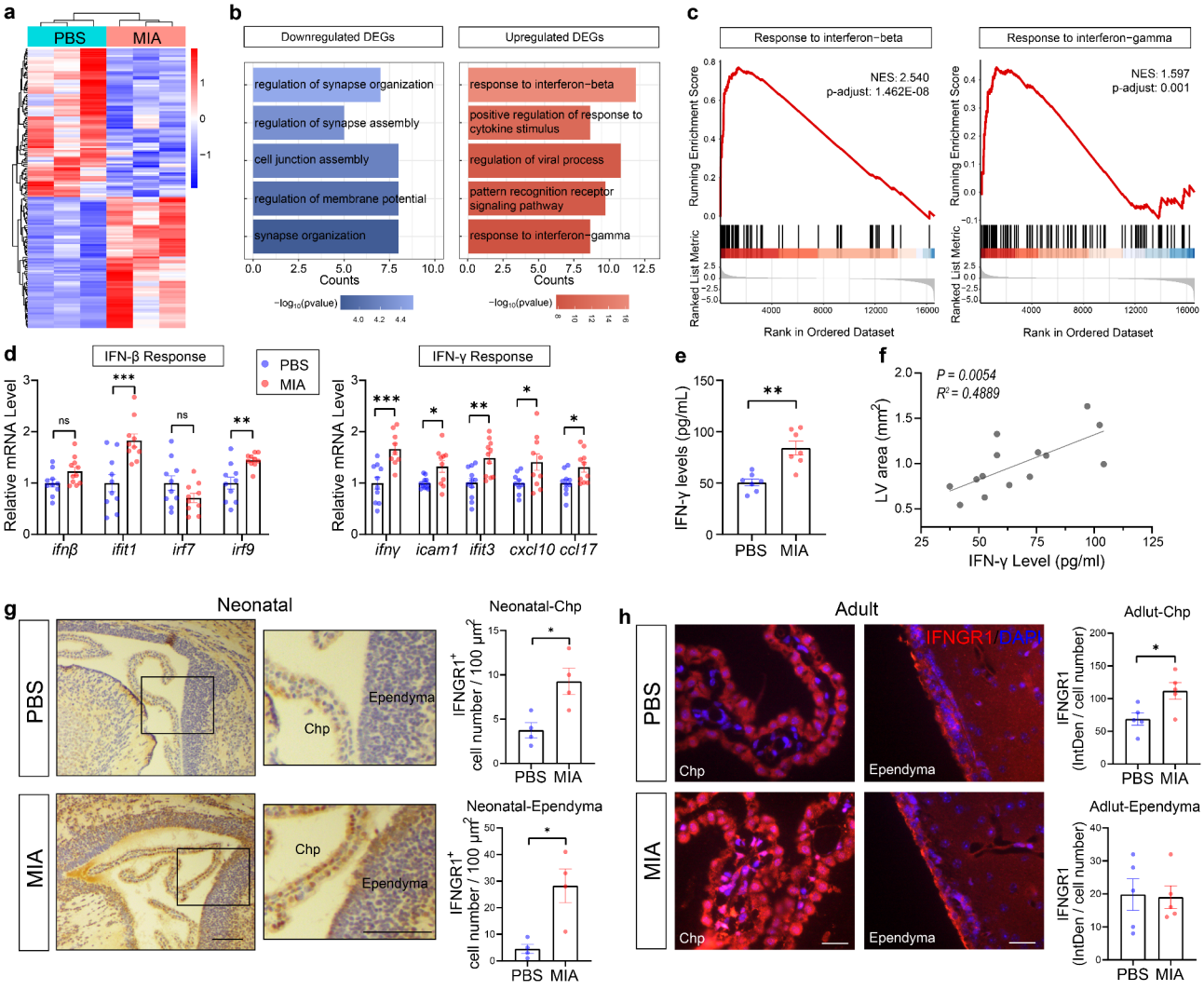

Fig. 3 Enhanced IFN-γ signaling in the brain and serum of MIA offspring. (**a**) Heatmaps of the DEGs in the Chp from PBS and MIA offspring ($n=3$ individual pools from 6 mice from 4 litters per group). (**b**) GO analysis of downregulated (blue) and upregulated (red) DEGs in the Chp of MIA offspring. (**c**) GSEA plots showing the enrichment of GO terms (response to IFN-β and response to IFN-γ) associated genes in MIA offspring compared with PBS offspring. (**d**) qPCR analysis of transcription levels of IFN-β and γ-related genes in the Chp of offspring ($n=9$–10 from 4 litters). Unpaired T tests were applied. * $P<0.05$, ** $P<0.01$, *** $P<0.001$. (**e**) ELISA analysis of IFN-γ levels in the serum of offspring ($n=7$ from 3–4 litters). Unpaired T tests were applied. ** $P<0.01$. (**f**) Correlation analysis between serum IFN-γ level and ventricle size in offspring ($n=14$ from 4–5 litters). (**g**) Representative IHC staining images of IFNGRl staining in the Chp and ependyma of neonatal offspring. Scale bars, 200 μm (low magnification), and 100 μm (high magnification). Quantification of IFNGR1-positive cells ($n=4$ from 3 litters). Unpaired T tests were applied. * $P<0.05$. (**h**) Representative IF staining images of IFNGR1 staining in the Chp and ependyma of adult offspring. Scale bars, 100 μm. Quantification of the fluorescence intensity of single cells ($n=5$ from 3–4 litters). Unpaired T tests were applied. * $P<0.05$

IFN-γ/Stat1 signaling impaired CHPE barrier function by activating macrophages

Our in vivo results demonstrated that the B-CSFB of MIA offspring was disrupted. Subsequently, we aimed to investigate the direct impact of IFN-γ in primary CHPEs. Following IFN-γ stimulation, there were no observable changes in the expression levels or distribution of the tight junction proteins occludin and β-catenin. These tight junction proteins remained intact and continuously distributed along the boundaries of each cell in control and IFN-γ groups (Fig. S5b–d). Similarly, we confirmed that the permeability of CHPEs exposed to IFN-γ remained unchanged through quantification of FITC-Dextran permeability (Fig. S5e). Furthermore, we observed a notable upregulation of intercellular adhesion molecule-1 (Icam1) in CHPEs in response to IFN-γ stimulation (Fig. S5b). This upregulation has the potential to facilitate the migration of immune cells across epithelial barriers [17, 41]. Collectively, these findings indicated that IFN-γ did not exert a direct influence on the permeability of CHPEs; instead, it enhanced the expression of adhesion molecules.

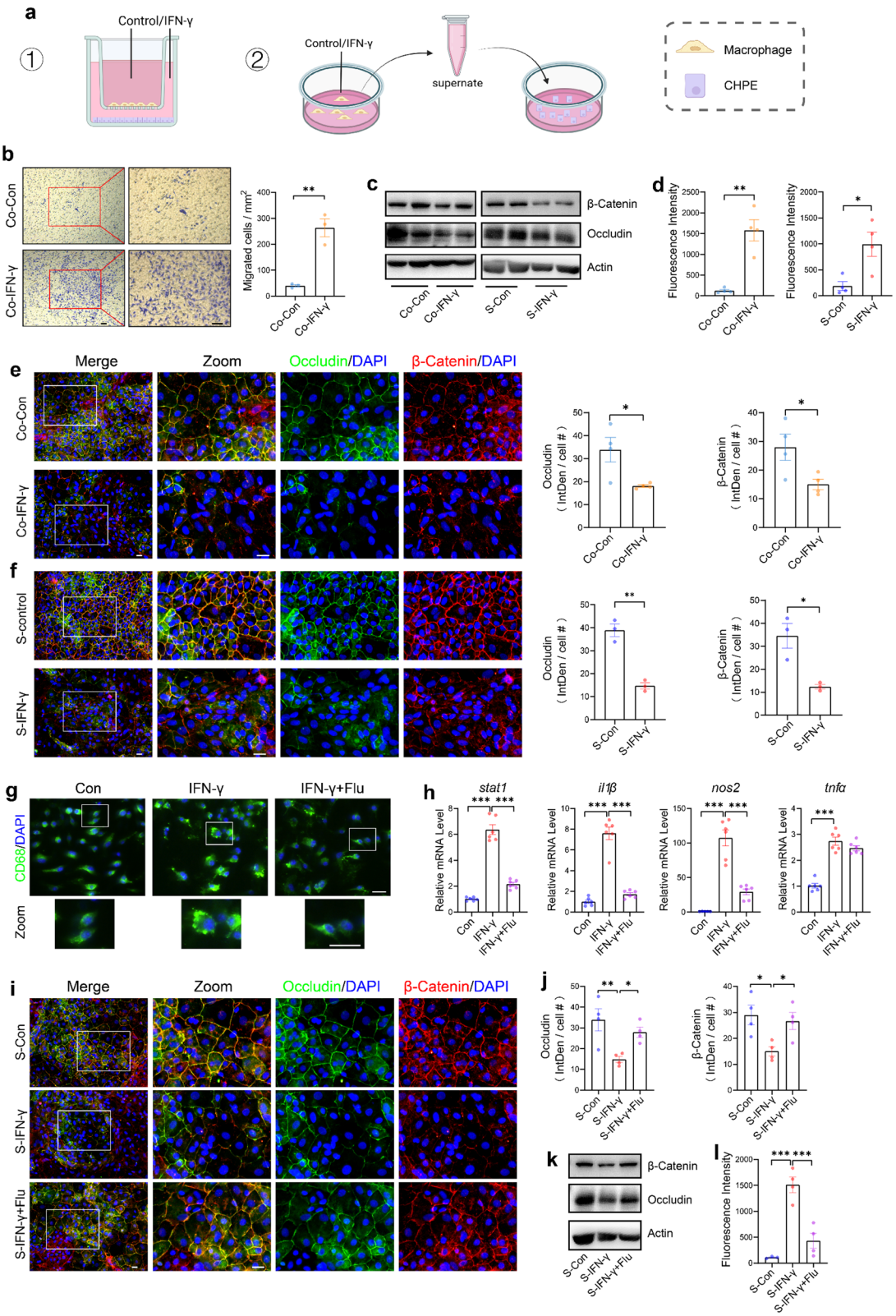

Fig. 4 (See legend on next page.)

(See figure on previous page.)

Fig. 4 IFN-γ activates macrophages through Stat1 to impair the barrier function of CHPEs. (**a**) Schematic diagram of two models include CHPEs co-cultured with macrophages (①) and macrophage-conditioned medium (②). ① shows the culture of CHPE and macrophages in the Transwell system. In the migration assay, macrophages were seeded in the upper chamber of the Transwell insert, while CHPE were seeded in the lower chamber (culture plate). In the leakage assay, the arrangement was reversed. ② shows the co-culture of CHPE and macrophages with conditioned medium supernatant. ① represents the co-culture models prefixed with "Co-", and ② represents the models prefixed with "S-" (**b**) Representative images of macrophage migration assay. Scale bars, 100 μm. Quantification of cells on the back of the chamber ($n=3$). Unpaired T tests were applied. ** $P<0.01$. (**c**) Representative immunoblots of Occludin and β-Catenin protein levels in CHPEs under two co-culture conditions. (**d**) Quantification of fluorescence intensity in the lower chamber medium for the two co-culture models ($n=4$). Unpaired T tests were applied. ** $P<0.01$ and * $P<0.05$. (**e**, **f**) Representative IF staining images and quantification of Occludin and β-Catenin fluorescence intensity in CHPEs co-cultured with macrophages (e) and macrophage-conditioned medium (f), ($n=3$–4). Scale bars, 50 μm. Unpaired T tests were applied. ** $P<0.01$ and * $P<0.05$. (**g**) Representative IF images of CD68 staining in macrophages. Scale bars, 50 μm. (**h**) qPCR analysis of stat1, il1β, nos2, and tnfα mRNA expression in macrophages ($n=6$). One-way ANOVA was applied. *** $P<0.001$. (**i** and **j**) Representative IF staining images (i) and quantification (j) of Occludin and β-Catenin fluorescence intensity in CHPEs ($n=4$). Scale bars, 50 μm. One-way ANOVA tests were applied. ** $P<0.01$ and * $P<0.05$. (**k**) Representative immunoblots of Occludin and β-Catenin protein levels in CHPEs. (**l**) Quantification of fluorescence intensity in the lower chamber medium for the conditioned medium co-culture model ($n=4$). One-way ANOVA tests were applied. *** $P<0.001$

Previous studies have identified macrophages as the main type of immune cells in Chp [38, 39]. An increase in infiltrating macrophages in Chp of MIA offspring was confirmed (Fig. 2f). We employed two indirect coculture models to further investigate whether IFN-γ impairs primary CHPEs through the mediation of macrophages. CHPEs were cocultured with macrophages in a Transwell system or culture medium of macrophages (Fig. 4a). In the Transwell system, we found that increased macrophages migrated to the back of the Transwell when cocultured with CHPEs stimulated with IFN-γ (Fig. 4b).

Subsequently, we examined CHPE barrier function alterations in both coculture models. Following IFN-γ stimulation, the distribution of occludin and β-catenin in CHPEs became diffuse and disrupted (Fig. 4e, f), while their expression levels decreased (Fig. 4c). The FITC-Dextran permeability test revealed an increase in CHPEs permeability in both IFN-γ-exposed coculture systems (Fig. 4d). These data demonstrated that IFN-γ impaired the barrier function of CHPEs by activating macrophages.

IFN-γ is known to activate a cascade of molecular events converging on the activation of signal transducer and activator of transcription 1 (Stat1) [42]. We utilized fludarabine (Flu), a drug that selectively inhibits Stat1, to evaluate the role of Stat1 in macrophage activation. CD68 staining revealed that oval- or spindle-shaped resting macrophages transformed into amoeba-like-activated cells with multiple pseudopodia upon IFN-γ stimulation. Importantly, Flu inhibited the activation and morphological changes in these macrophages (Fig. 4g). Furthermore, we found that Flu reduced the mRNA level of Stat1, nitric oxide synthase 2 (Nos2), and interleukine-1 β (IL-1β), which increased in IFN-γ-induced macrophages (Fig. 4h). In the supernatant of the macrophage culture medium coculture systems, we found Flu recovered IFN-γ-induced impairment in the expression and distribution of CHPEs (Fig. 4i–k). Furthermore, the FITC-Dextran leakage of CHPEs decreased during Flu treatment (Fig. 4l). Together, our findings indicated that IFN-γ triggered a pro-inflammatory state in macrophages by activating Stat1, leading to their migration and subsequent disruption of the CHPE barrier function.

IFN-γ/Stat1 signaling suppressed EC differentiation by inhibiting Stat3 activation

Our results indicated elevated IFNGR1 expression in ependyma of MIA offspring during the neonatal period (Fig. 3g), accompanied by reduced ventricular zone cell density in adulthood (Fig. 2n, p). These data suggest aberrant differentiation of ECs in MIA offspring during early development, potentially due to IFN-γ signaling interference. IFN-γ signaling plays a crucial role in neuronal development, influencing neural progenitor cells and oligodendrocyte progenitor cell differentiation [43, 44]. However, much less is known about the effect of IFN-γ on EC differentiation. To investigate this effect, we treated primary ECs with IFN-γ daily from day 1 (D1) to day 7 (D7) of the differentiation process. The number of multiciliated ECs (Ace. Tub-positive cells) and Foxj1-positive cells significantly decreased on D7 after IFN-γ stimulation (Fig. 5a, b), indicating that IFN-γ directly suppressed EC differentiation. Further, we observed a reduction in both Foxj1 protein and mRNA expression levels in ECs treated with IFN-γ, starting from D3 (Fig. 5c).

We then sought to uncover the underlying mechanisms responsible for this effect. Stimulation of IFN-γ resulted in enhanced Stat1 levels and phosphorylation of the Stat1 (at tyrosine 701, denoted as pStat1) on D1, which was prior to the diminished expression of Foxj1 (Fig. 5e). This finding confirmed an early activation of Stat1 in primary ECs in response to IFN-γ treatment. To elucidate the role of Stat1 signaling in the suppression of primary EC differentiation by IFN-γ, we treated IFN-γ stimulated ECs with Flu and found that inhibiting Stat1 reversed the reduction in Foxj1 on D3. IF analysis further confirmed that Flu reversed the reduction of mature multiciliated ECs induced by IFN-γ (Fig. 5f, g). These findings suggested that the inhibitory effect of IFN-γ on EC differentiation is dependent on Stat1 activation.

Next, we aimed to determine whether phosphorylated Stat1 translocated to the nucleus to regulate the transcription of Foxj1. First, we overexpressed Stat1 in HEK293T cells and confirmed an increase in Stat1 phosphorylation (Fig. 5h) and transfected a luciferase plasmid that carried the full-length promoter sequence of Foxj1. We found that the activation of Stat1 did not affect the transcriptional activity of the Foxj1 promoter (Fig. 5i), suggesting that Foxj1 is not directly targeted by Stat1 [45–47].

While previous studies have shown a reciprocal inhibitory relationship between Stat1 and signal transducer and activator of transcription 3 (Stat3) activation under specific inflammatory conditions, recent reports have also emphasized that Stat3 promotes the differentiation of airway multiciliated ECs through direct regulation of Foxj1 transcription. Consequently, we found that IFN-γ attenuated the phosphorylation of Stat3 in ECs (Fig. 5j), whereas Flu treatment restored phosphorylation of Stat3 (Fig. 5k), suggesting that IFN-γ/Stat1 signaling suppressed EC differentiation via Stat3.

Subsequently, we found that Stattic, an inhibitor of Stat3, abolished the restorative effect of Flu on the differentiation of ECs stimulated by IFN-γ, resulting in the inhibition of Foxj1 protein expression and a decrease in the number of multiciliated ECs (Fig. 5k, l). These results demonstrated that IFN-γ exerted an inhibitory effect on EC differentiation by suppressing the activation of Stat3 through Stat1.

IFN-γ signaling induced ventriculomegaly and ASD-like behavioral phenotypes in MIA offspring

To validate the critical involvement of IFN-γ signaling in MIA-induced developmental disorders, we tested whether blocking IFN-γ signaling would mitigate the effect of MIA on ventriculomegaly and ASD-like behavioral phenotypes of adult offspring. Specifically, pregnant dams were pretreated with IFNGR-blocking antibodies (anti-) or IgG at a dose of 500 μg per mouse via intraperitoneal injection 6 h before poly(I: C) or PBS injection on E12.5 (Fig. 6a). The MRI scans and behavioral tests revealed that maternal treatment with anti-IFNGR before poly (I: C) diminished the ventriculomegaly and ASD-like behaviors in adult MIA offspring (Fig. 6b, c). Furthermore, we also found that blocking the IFN-γ signaling restored the function and structure of Chp and ependyma in MIA offspring. Specifically, in Chp, maternal anti-IFNGR treatment reversed the MIA-induced hyperproduction of CSF and leakage of B-CSFB (Fig. 6d, e). Furthermore, blocking IFN-γ signaling restored normal NKCC1 activation, reduced macrophage infiltration, and prevented the disruption of tight junction proteins (Fig. 6f–k). In ependyma, the weakened CSF flow and abnormal EC distribution in MIA offspring were alleviated upon maternal anti-IFNGR treatment (Fig. 6l–r, Fig. S2). Taken together, these data indicated that maternal IFN-γ signaling is crucial for mediating the MIA-induced ventriculomegaly and ASD-like behaviors in adult offspring.

To further determine the direct effect of IFN-γ on the ventriculomegaly and behavior of adult offspring, we injected IFN-γ recombinant protein or PBS into pregnant dams on E12.5 (Fig. 7a). Similar to poly (I: C) injection, maternal IFN-γ injection resulted in ventriculomegaly and ASD-like phenotypes in adult offspring (Fig. 7b, c). In Chp, maternal IFN-γ injection also increased the CSF production and Chp permeability in offspring (Fig. 7d, e). Furthermore, the inflammatory damage of Chp characterized by macrophage infiltration, activation of NKCC1, and disrupted tight junction was also found following maternal IFN-γ injection (Fig. 7f–k). In ependyma, maternal IFN-γ injection slowed ependymal cilia-generated CSF flow and decreased the density of ECs and cilia at LVs of offspring (Fig. 7l–r, Fig. S2). Together, these data demonstrated that, similar to MIA, prenatal exposure to IFN-γ is sufficient to trigger ventriculomegaly and ASD-like behaviors in adult offspring.

Discussion

In this study, we demonstrated that impaired Chp and ependyma caused by enhanced IFN-γ signaling led to ventriculomegaly in MIA offspring. First, we found that male offspring exhibited ventriculomegaly due to Chp and ependyma impairments using the MIA model. Bulk RNA-seq and further experiments confirmed that IFN-γ signaling was enhanced in adult MIA offspring. In vitro, IFN-γ signaling could disrupt the CHPE barrier function and EC differentiation. Neutralizing IFN-γ signaling alleviated Chp and ependyma dysfunction, ventriculomegaly, and ASD-like behaviors in adult MIA offspring. Additionally, elevated IFN-γ signaling in normal pregnant mice mimicked MIA-induced impairments in adult offspring. Overall, these findings not only elucidate the potential link between IFN-γ signaling and ventriculomegaly in ASD but also provide valuable insights into the complex relationship between transient inflammation and neurodevelopmental disorders.

Of particular relevance, ventriculomegaly has been reported in children with ASD, and a significant correlation between ventriculomegaly in children with ASD and various behavioral deficiencies was found [14]. Our study is the first demonstration of ventriculomegaly present in MIA offspring. Also, we indicated a significant positive correlation between ventriculomegaly and ASD-like behaviors in adult MIA offspring. However, a definitive causal link between ventricular enlargement and ASD remains elusive. Ventriculomegaly is widely regarded as a consequence of CSF circulation dysfunction.

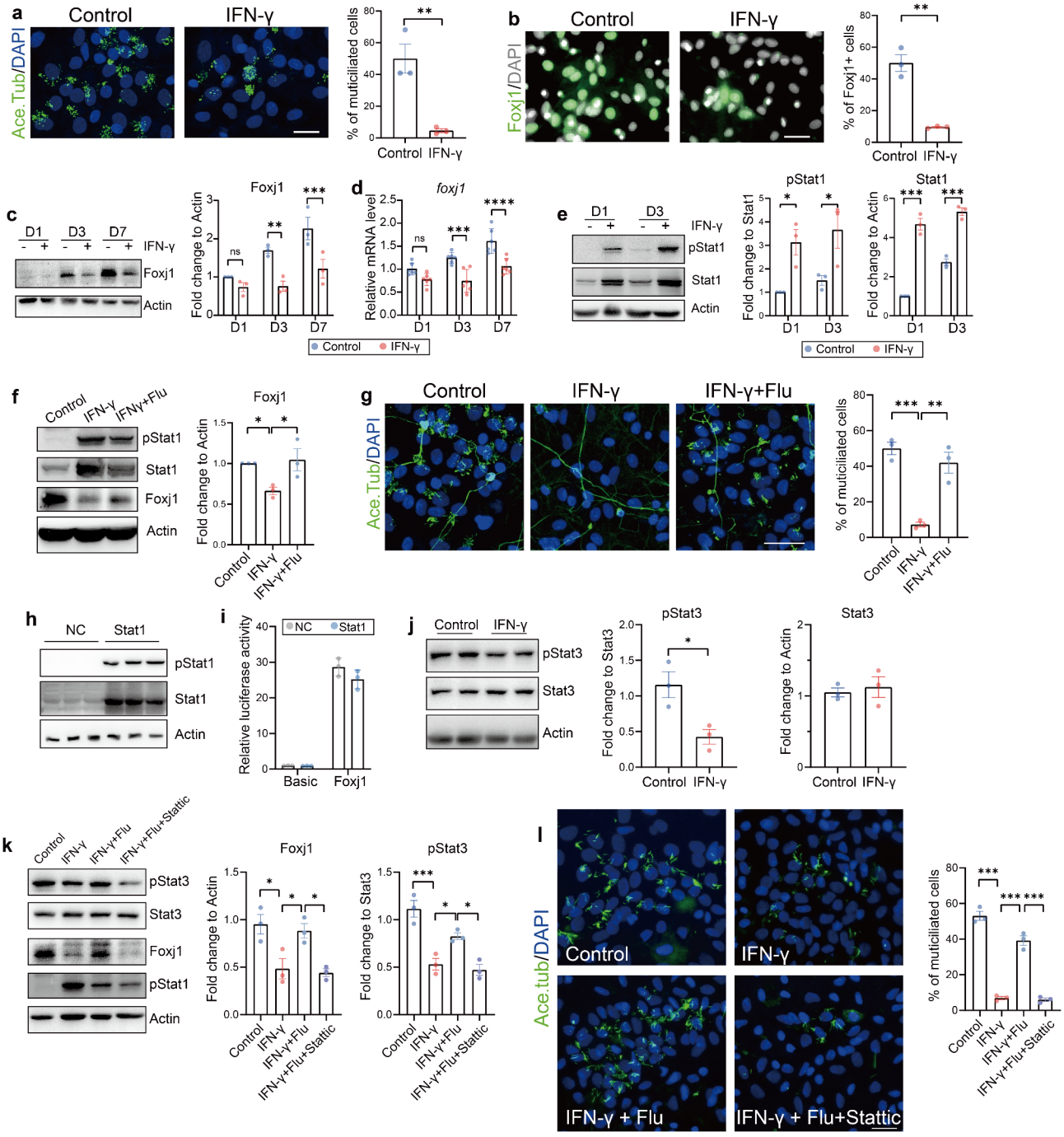

Fig. 5 IFN-γ inhibits Stat3 activation through Stat1 to block the differentiation of primary ECs. (**a**) Representative IF images of Ace. Tub staining and quantification of multiciliated ECs ($n=3$). Scale bars, 50 μm. Unpaired T tests were applied. * $P<0.05$. (**b**) Representative IF images and quantification of Foxj1-positive ECs ($n=3$). Scale bars, 100 μm. Unpaired T tests were applied. ** $P<0.01$. (**c**) Representative immunoblot images and quantification of Foxj1 protein levels on D1, 3, and 7 of EC differentiation ($n=3$). Two-way ANOVA tests were applied. ** $P<0.01$ and *** $P<0.001$. (**d**) qPCR analysis of foxj1 mRNA levels on D1, 3, and 7 of EC differentiation ($n=6$). Two-way ANOVA tests were applied. *** $P<0.001$ and **** $P<0.0001$. (**e**) Representative immunoblot images and quantification of Stat1 protein expression and phosphorylation activation on D1 and 3 of EC differentiation ($n=3$). Two-way ANOVA tests were applied. * $P<0.05$ and *** $P<0.001$. (**f**) Representative immunoblot images of pStat1, Stat1, and Foxj1 protein levels in ECs, with representative images and statistical results for Foxj1 ($n=3$). One-way ANOVA tests were applied. * $P<0.05$. (**g**) Representative IF images of Ace. Tub staining and quantification of multiciliated ECs ($n=3$). Scale bars, 100 μm. One-way ANOVA tests were applied. ** $P<0.01$ and *** $P<0.001$. (**h**) Representative immunoblot images of Stat1 protein levels and phosphorylation activation in HEK293T cells ($n=3$). (**i**) Quantification of the luciferase activity in HEK293T cells ($n=3$). Two-way ANOVA tests were applied. (**j**) Representative immunoblot images and quantification of pStat3 and Stat3 expression levels in ECs ($n=3$). Unpaired T tests were applied. * $P<0.05$. (**k**) Representative immunoblot images and quantification of pStat3 and Foxj1 protein expression levels in ECs ($n=3$). One-way ANOVA tests were applied. * $P<0.05$ and *** $P<0.001$. (**l**) Representative IF images of Ace. Tub staining and quantification of multiciliated ECs. Scale bars, 100 μm. ($n=3$). One-way ANOVA tests were applied. *** $P<0.001$

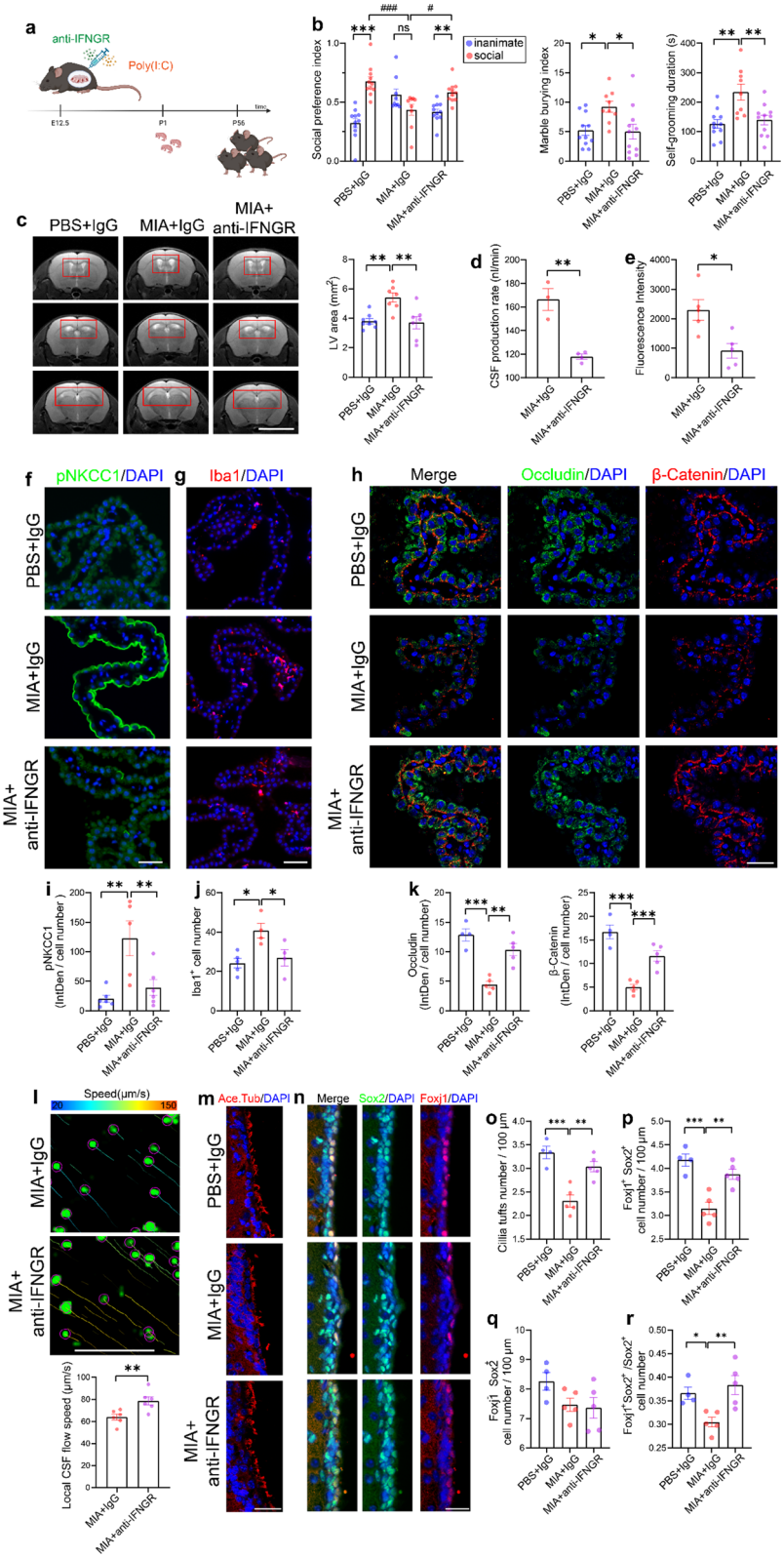

Fig. 6 (See legend on next page.)

(See figure on previous page.)

Fig. 6 Blocking maternal IFN-γ signaling mitigates the effects of MIA on offspring. (**a**) Schematic diagram of the experimental design. Pregnant dams were pretreated with IFNGR-blocking antibodies (anti-IFNGR) or IgG before injecting Poly (I: C) or PBS on E12.5. (**b**) Statistical graphs of ASD-like behaviors in offspring, including three-chamber social test, grooming test, and marble burying test ($n = 9$–11 from 4–5 litters). Two-way ANOVA tests (for the three-chamber social test) and Unpaired T tests (for grooming and marble burying tests) were applied. *** $P < 0.001$, ** $P < 0.01$, * $P < 0.05$, ### $P < 0.001$, # $P < 0.05$ and ns $P > 0.05$. (**c**) Representative MRI images and quantification of LVs areas in offspring ($n = 7$–8 from 4–5 litters). Scale bar, 5 mm. One-way ANOVA tests were applied. ** $P < 0.01$. (**d**) Quantification of CSF production rate in offspring ($n = 3$–4 from 3 litters). Unpaired T tests were applied. ** $P < 0.01$. (**e**) Quantification of the CSF fluorescence intensity in offspring from the B-CSFB assessment ($n = 5$ from 3–4 litters). Unpaired T tests were applied. * $P < 0.05$. (**f** and **i**) Representative IF staining images (**f**) and quantification (i) pNKCC1 fluorescence intensity in the Chp of offspring ($n = 5$–6 from 3–4 litters). Scale bar, 100 μm. One-way ANOVA tests were applied. * $P < 0.05$. (**g** and **j**) Representative IF staining images (**g**) and quantification (**j**) of $Iba1^+$ macrophage in the Chp of offspring ($n = 4$–6 from 3–4 litters). Scale bar, 100 μm. One-way ANOVA tests were applied. ** $P < 0.01$. (h and k) Representative IF staining images (h) and quantification (h) of Occludin and β-Catenin fluorescence intensity in the Chp of offspring ($n = 4$–5 from 3–4 litters). Scale bar, 100 μm. One-way ANOVA tests were applied. ** $P < 0.01$ and *** $P < 0.001$. (l) Representative images of fluorescent microsphere trajectories. Scale bar, 100 μm. Quantification of fluorescent microsphere movement speed in the LVs of offspring ($n = 6$, from 3 litters per group). Unpaired T tests were applied. ** $P < 0.01$. (m and o) Representative IF staining images (**m**) and quantification (**o**) of ciliary tufts in the LVs of offspring ($n = 4$–5 from 3 litters). Scale bar, 100 μm. One-way ANOVA tests were applied. *** $P < 0.001$, ** $P < 0.01$. (**n**-**r**) Representative IF staining images of ECs in the lateral ventricles of offspring (**n**). Scale bar, 100 μm. Quantification of the density of $Foxj1^+Sox2^+$ ECs (p) and $Foxj1^-Sox2^+$ neural progenitor cells (q) and the ratio of the two (r), ($n = 5$–6 from 3–4 litters). Unpaired T tests were applied. ** $P < 0.01$ and * $P < 0.05$

Abnormalities in CSF dynamics and components can further precipitate functional deficits associated with the brain parenchyma [48–50]. In cases of CSF accumulation induced by infection or hemorrhage, the elevated levels of hemoglobin and inflammatory factors, coupled with the diminished neurotrophic factors in the CSF, directly engaged with neurons and glial cells, thereby eliciting gray matter injury and neuroinflammatory reactions [51–53]. Conversely, researchers have also highlighted the importance of precisely regulated early neurodevelopment for normal brain–CSF biomechanics [54, 55]. Structural abnormalities of the ventricular wall stemming from neurodevelopmental disorders can disrupt normal CSF circulation by influencing CSF turbulence. The resulting ventriculomegaly due to abnormal CSF circulation can concurrently impact neurogenesis or neuroregeneration in the SVZ, thereby further influencing neural function [56, 57]. This suggests a bidirectional causal relationship between neurodevelopmental disorders and ventriculomegaly, where each condition can both initiate and reinforce the other.

To investigate the mechanism underlying ventriculomegaly in MIA offspring, we conducted bulk RNA-seq and found enhanced IFN-γ signaling in adult MIA offspring, which was confirmed in further experiments in vivo. MIA induces an upregulation of multiple inflammatory cytokines in the maternal body, including IL-6, IL-1β, TNF-α, and the focus of our study, IFN-γ [6]. These cytokines impair neurodevelopment through various pathways. The interaction between IFN-γ and other cytokines is quite complex. Previous studies have shown that Poly(I: C) promotes the production of IL-12 and IFN-α/β by activating the TRL3 of immune cells, which in turn act on NK cells and T cells to indirectly promote the generation of IFN-γ [58, 59]. The production of IFN-γ further stimulates other immune cells to release IL-1β and TNF-α, amplifying the proinflammatory signal. Additionally, IL-6 and IFN-γ have been reported to mutually induce each other's production [60, 61]. However, in some studies, IFN-γ also inhibits IL-6 signaling through certain downstream transcription factors, exerting a negative feedback regulatory effect [62]. Therefore, within the context of the MIA model, there exist both synergistic and inhibitory interactions among IFN-γ and other elevated inflammatory cytokines. Our findings indicate that IFN-γ not only induces the infiltration of inflammatory cells and impairs the barrier function of the choroid plexus, but also directly inhibits the differentiation of ependymal cells. However, the synergistic effects of other inflammatory factors with IFN-γ, as well as their detrimental impact on the neurodevelopment of MIA offspring, should not be overlooked and warrants further investigation.

IFN-γ was reported to activate immune cells and stimulate chemokine expression in the CNS border, such as Chp, subsequently promoting immune cell infiltration into CNS [17, 41]. Similarly, our findings confirmed an elevated macrophage infiltration in Chp of adult MIA offspring, and we further validated that IFN-γ enhanced the migration of macrophages toward CHPEs, ultimately compromising their barrier function. In addition to Chp, mLVs have been recently identified as a hotspot for draining CSF and immune cells. Interestingly, diminished lymphatic drainage was found in adult MIA offspring, potentially due to reduced functional protein expression within their lymphatic vessels. In previous studies, it has been discovered that IFN-γ can directly impair the tube formation and barrier function of lymphatic endothelial cells (LECs) at the in vitro level [63, 64]. Furthermore, the IFN-γ signal serves as a key signaling mechanism for T-cell-based immunotherapy to induce LEC apoptosis and reduce tumor lymphatic vessel density [65, 66]. Considering that mLVs also belong to the lymphatic vessel system, we speculate that the elevated IFN-γ signal in MIA offspring mice may also affect the function of their mLVs through the aforementioned mechanisms.

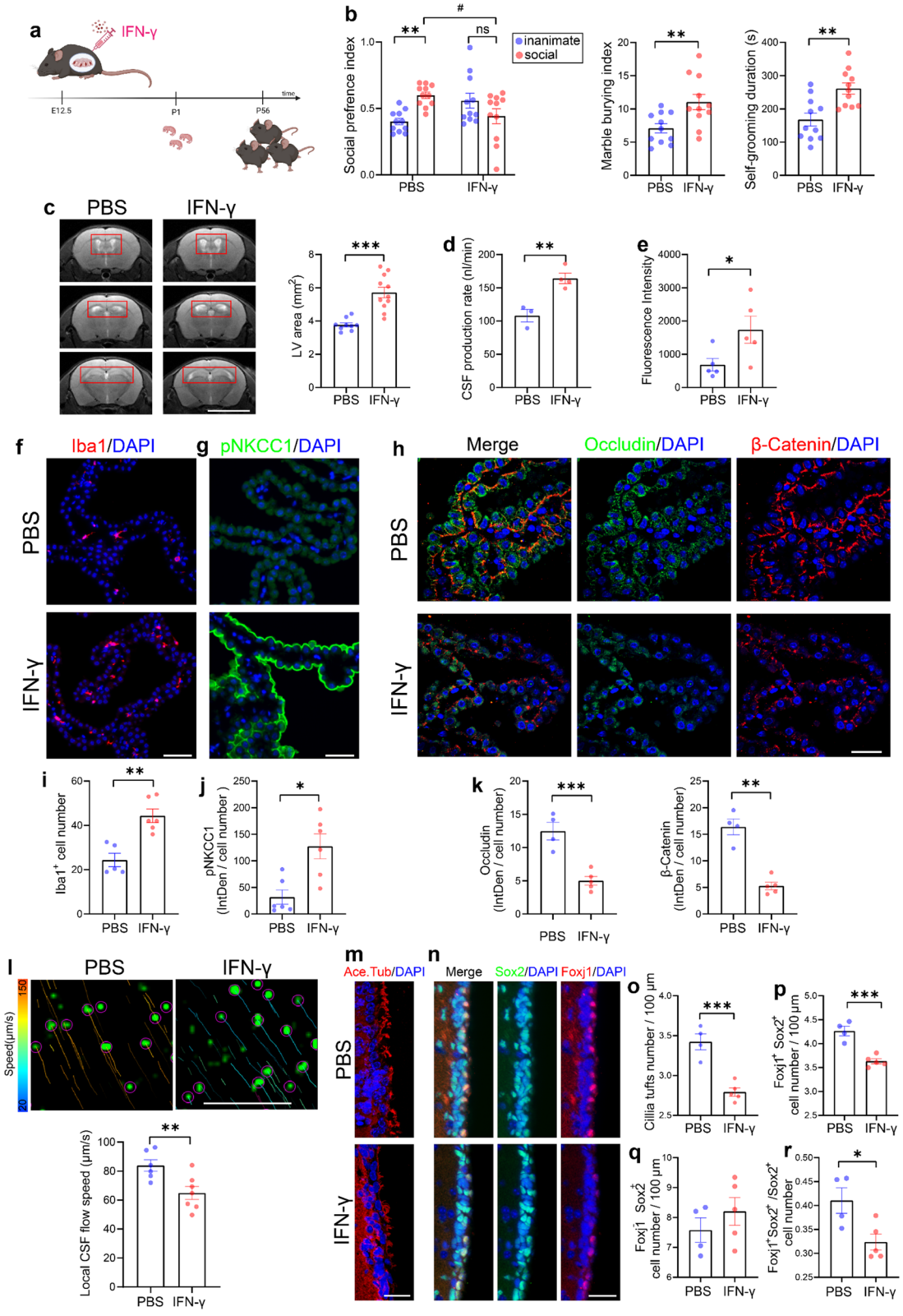

Fig. 7 (See legend on next page.)

(See figure on previous page.)

Fig. 7 Elevated maternal IFN-γ signaling triggers ventriculomegaly, ASD-like behaviors, and Chp and ependyma dysfunction in offspring. (**a**) Schematic diagram of the experimental design. Pregnant C57BL/6 mice were i.p. injected with IFN-γ recombinant protein or vehicle (PBS) on E12.5. (**b**) Statistical graphs of ASD-like behaviors in offspring, including three-chamber social test, grooming test, and marble burying test ($n = 10–11$ from 4–5 litters). Two-way ANOVA tests (for the three-chamber social test) and Unpaired T-tests (for grooming and marble burying tests) were applied. ** $P < 0.01$, # $P < 0.05$ and ns $P > 0.05$. (**c**) Representative MRI images and quantification of LVs areas in offspring ($n = 9–11$ from 4–5 litters). Scale bar, 5 mm. Unpaired T tests were applied. *** $P < 0.001$. (**d**) Quantification of CSF production rate in offspring ($n = 3–4$ from 3 litters). Unpaired T tests were applied. ** $P < 0.01$. (**e**) Quantification of the CSF fluorescence intensity in offspring from the B-CSFB assessment ($n = 5$ from 3 litters). Unpaired T tests were applied. * $P < 0.05$. (**f** and **i**) Representative IF staining images (f) and quantification (i) of Iba1$^+$ macrophage in the Chp of offspring ($n = 5–6$ from 3–4 litters). Scale bar, 100 μm. Unpaired T tests were applied. ** $P < 0.01$. (**g** and **j**) Representative IF staining images (g) and quantification (j) pNKCC1 fluorescence intensity in the Chp of offspring ($n = 6$ from 3–4 litters). Scale bar, 100 μm. Unpaired T tests were applied. * $P < 0.05$. (**h** and **k**) Representative IF staining images (h) and quantification (h) of Occludin and β-Catenin fluorescence intensity in the Chp of offspring ($n = 4–5$ from 3 litters). Scale bar, 100 μm. Unpaired T tests were applied. ** $P < 0.01$ and *** $P < 0.001$. (**l**) Representative images of fluorescent microsphere trajectories. Scale bar, 100 μm. Quantification of fluorescent microsphere movement speed in the LVs of offspring ($n = 6–7$, from 3–4 litters per group). Unpaired T tests were applied. ** $P < 0.01$. (**m** and **o**) Representative IF staining images (m) and quantification (o) of ciliary tufts in the LVs of offspring ($n = 4–5$ from 3 litters). Scale bar, 100 μm. Unpaired T tests were applied. *** $P < 0.001$. (**n**-**r**) Representative IF staining images of ECs in the lateral ventricles of offspring (n). Scale bar, 100 μm. Quantification of the density of Foxj1$^+$Sox2$^+$ ECs (**p**) and Foxj1$^-$Sox2$^+$ neural progenitor cells (**q**) and the ratio of the two (r), ($n = 5–6$ from 3–4 litters). Unpaired T tests were applied. *** $P < 0.001$ and * $P < 0.05$

However, the specific mechanism requires further exploration.

Compared to Chp and meninges, ependyma does not have direct contact with the peripheral immune system. Previous studies have revealed that microglial or complement system activation can impair EC survival and differentiation in neuroinflammatory models [67–69]. Our study further identified structural and functional abnormalities in ECs of adult MIA offspring, with enhanced IFN-γ signaling blocking EC differentiation. These findings provide a novel perspective for exploring the pathological injury mechanisms of ECs in neuroinflammatory disorders. Ependymal differentiation in MIA offspring, notably, is potentially linked to factors beyond IFN-γ, as evidenced by the activated microglia and abnormal neuroregulatory functions in Chp, identified through gene sequencing and GO-enrichment analysis.

There are still some limitations in our research. Firstly, while we have established that MIA can lead to ventricular dilation in offspring, the specific causal nexus between ASD and ventriculomegaly remains an area ripe for deeper investigation. Secondly, our confirmation that ventricular dilation in MIA offspring mice stems from dysfunction of the choroid plexus and ependyma prompts the need for additional research into whether mLV dysfunction plays a direct role in MIA-induced ventriculomegaly. Furthermore, the involvement of other pathways regulating CSF circulation, such as the glial lymphatic system and vascular system, also necessitates meticulous examination. Thirdly, although we have observed the impaired function of the B-CSFB in offspring mice through the dye leakage experiment, more advanced techniques (such as two-photon imaging) are still needed to visualize the dye leakage process, so as to exclude the interference from other pathways such as the blood-brain barrier and circumventricular organs. Lastly, despite our successful use of IFN-γ neutralizing antibodies to ameliorate ventriculomegaly and ASD-like behaviors in offspring, the practical application of these antibodies is hindered by challenges such as a narrow therapeutic window, a prolonged half-life, suboptimal targeting specificity, and elevated treatment costs. Consequently, there is a pressing need to identify an effective alternative drug that can attenuate or block IFN-γ signaling in both mothers and offspring.

In summary, this study revealed the role and mechanism of IFN-γ signaling in ventriculomegaly of MIA offspring. Our findings provide new insights into the pathological mechanisms of ASD and identify a potential therapeutic target for the treatment of neurodevelopmental disorders.

Abbreviations

ASD	Autism Spectrum Disorder
MIA	Maternal Immune Activation
IFN	Interferon
Chp	Choroid Plexus
SVZ	Subventricular Zone
CHPE	Chp Epithelial Cell
LV	Lateral Ventricle
B-CSFB	Blood-CSF Barrier
Stat1	Signal Transducer and Activator of Transcription 1
Flu	Fludarabine

Supplementary Information

The online version contains supplementary material available at https://doi.org/10.1186/s12974-025-03409-3.

Supplementary Material 1

Supplementary Material 2

Acknowledgements

Not applicable.

Author contributions

Y.-Q.S. was involved in performing experiments, analysis, and interpretation of data and writing the paper. X.-X.H. performed the experiments and were involved in the acquisition and interpretation of the data and made significant contributions to the revised manuscript. In addition, W.G., C.H., and J.J. performed part experiments and were involved in the acquisition and interpretation of the data. X.-Y.Z., J.J., and J.Y. participated in the experiments. G.H. was involved in conception and acquisition. X.-L.S. was involved in the conception and design, acquisition, and writing the paper and final approval of the version to be submitted. All authors approved the final manuscript.

Funding
This study was supported by the National Key Research and Development Program of China (No. 2021ZD0202901), the National Natural Science Foundation of China (No. 82373848, 82304479, and 81973301), and the Medical Research Project of Jiangsu Commission of Health (No. ZDA2020006) for funding.

Data availability
The datasets generated during the current study are available from the corresponding authors on reasonable request.

Declarations

Ethics approval and consent to participate
All animal experimental protocols and procedures were approved by the Nanjing Medical University Experimental Animal Ethics Committee (2004037-1) and complied with the guidelines for the use of experimental animals.

Consent for publication
Not applicable.

Competing interests
The authors declare no competing interests.

Received: 24 December 2024 / Accepted: 5 March 2025
Published online: 15 March 2025

References

1. Hirota T, King BH. Autism spectrum disorder. JAMA. 2023;329:157.
2. HY J, LL X, RM LS, ZH X, ZX Y. L, Maternal infection during pregnancy and risk of autism spectrum disorders: A systematic review and meta-analysis. Brain Behav Immun. 2016;58.
3. Atladóttir HÓ, Henriksen TB, Schendel DE, Parner ET. Autism after infection, febrile episodes, and antibiotic use during pregnancy: an exploratory study. Pediatrics. 2012;130:e1447–54.
4. Estes ML, Mcallister AK. Maternal immune activation: Implications for neuropsychiatric disorders. 2016;353.
5. Brown AS, Begg MD, Gravenstein S, Schaefer CA, Wyatt RJ, Bresnahan M, et al. Serologic evidence of prenatal influenza in the etiology of schizophrenia. Arch Gen Psychiatry. 2004;61:774–80.
6. Hughes HK, Moreno RJ, Ashwood P. Innate immune dysfunction and neuroinflammation in autism spectrum disorder (ASD). Focus (Am Psychiatr Publ). 2024;22:229–41.
7. Cui J, Shipley FB, Shannon ML, Alturkistani O, Dani N, Webb MD, et al. Inflammation of the embryonic choroid plexus barrier following maternal immune activation. Dev Cell. 2020;55:617–e6286.
8. Loayza M, Lin S, Carter K, Ojeda N, Fan L-W, Ramarao S, et al. Maternal immune activation alters fetal and neonatal microglia phenotype and disrupts neurogenesis in mice. Pediatr Res. 2023;93:1216–25.
9. Ben-Reuven L, Reiner O. Dynamics of cortical progenitors and production of subcerebral neurons are altered in embryos of a maternal inflammation model for autism. Mol Psychiatry. 2021;26:1535–50.
10. Damkier HH, Brown PD, Praetorius J. Cerebrospinal fluid secretion by the choroid plexus. Physiol Rev. 2013;93:1847–92.
11. Robert SM, Reeves BC, Kiziltug E, Duy PQ, Karimy JK, Mansuri MS, et al. The choroid plexus links innate immunity to CSF dysregulation in hydrocephalus. Cell. 2023;186:764–e78521.
12. SA R, M F-O, K O MAN, L L-M JIP et al. Development of ependymal and postnatal neural stem cells and their origin from a common embryonic progenitor. Cell Rep. 2019;27.
13. Del Bigio MR. Ependymal cells: biology and pathology. Acta Neuropathol. 2010;119:55–73.
14. Kyriakopoulou V, Davidson A, Chew A, Gupta N, Arichi T, Nosarti C, et al. Characterisation of ASD traits among a cohort of children with isolated fetal ventriculomegaly. Nat Commun. 2023;14:1550.
15. MD S, CW N, DD L, K AL. A, RW E, Extra-axial cerebrospinal fluid in high-risk and normal-risk children with autism aged 2–4 years: a case-control study. Lancet Psychiatry. 2018;5.
16. Ortiz-Álvarez G, Daclin M, Shihavuddin A, Lansade P, Fortoul A, Faucourt M, et al. Adult neural stem cells and multiciliated ependymal cells share a common lineage regulated by the Geminin family members. Neuron. 2019;102:159–e1727.
17. Kunis G, Baruch K, Rosenzweig N, Kertser A, Miller O, Berkutzki T, et al. IFN-γ-dependent activation of the brain's choroid plexus for CNS immune surveillance and repair. Brain. 2013;136:3427–40.
18. Choi GB, Yim YS, Wong H, Kim S, Kim H, Kim SV et al. The maternal interleukin-17a pathway in mice promotes autism-like phenotypes in offspring. Science (1979). 2016;351:933–9.
19. GB C, YS Y, SV HWSKHK. K, The maternal interleukin-17a pathway in mice promotes autism-like phenotypes in offspring. Science. 2016;351.
20. Ben-Yehuda H, Matcovitch-Natan O, Kertser A, Spinrad A, Prinz M, Amit I, et al. Maternal Type-I interferon signaling adversely affects the microglia and the behavior of the offspring accompanied by increased sensitivity to stress. Mol Psychiatry. 2020;25:1050–67.
21. Shin Yim Y, Park A, Berrios J, Lafourcade M, Pascual LM, Soares N, et al. Reversing behavioural abnormalities in mice exposed to maternal inflammation. Nature. 2017;549:482–7.
22. Liu G, Mestre H, Sweeney AM, Sun Q, Weikop P, Du T, et al. Direct measurement of cerebrospinal fluid production in mice. Cell Rep. 2020;33:108524.
23. Grimes DT, Boswell CW, Morante NFC, Henkelman RM, Burdine RD, Ciruna B. Zebrafish models of idiopathic scoliosis link cerebrospinal fluid flow defects to spine curvature. Science. 2016;352:1341–4.
24. Bolte AC, Dutta AB, Hurt ME, Smirnov I, Kovacs MA, McKee CA, et al. Meningeal lymphatic dysfunction exacerbates traumatic brain injury pathogenesis. Nat Commun. 2020;11:4524.
25. Strahle J, Garton HJL, Maher CO, Muraszko KM, Keep RF, Xi G. Mechanisms of hydrocephalus after neonatal and adult intraventricular hemorrhage. Transl Stroke Res. 2012;3:25–38.
26. Proulx ST. Cerebrospinal fluid outflow: a review of the historical and contemporary evidence for arachnoid Villi, perineural routes, and dural lymphatics. Cell Mol Life Sci. 2021;78:2429–57.
27. Duy PQ, Greenberg ABW, Butler WE, Kahle KT. Rethinking the cilia hypothesis of hydrocephalus. Neurobiol Dis. 2022;175:105913.
28. Kahle KT, Kulkarni AV, Limbrick DD, Warf BC. Hydrocephalus in children. Lancet. 2016;387:788–99.
29. Karimy JK, Reeves BC, Damisah E, Duy PQ, Antwi P, David W, et al. Inflammation in acquired hydrocephalus: pathogenic mechanisms and therapeutic targets. Nat Rev Neurol. 2020;16:285–96.
30. Karimy JK, Zhang J, Kurland DB, Theriault BC, Duran D, Stokum JA, et al. Inflammation-dependent cerebrospinal fluid hypersecretion by the choroid plexus epithelium in posthemorrhagic hydrocephalus. Nat Med. 2017;23:997–1003.
31. Galea I. The blood–brain barrier in systemic infection and inflammation. Cell Mol Immunol. 2021;18:2489–501.
32. Seyfert S, Becher A, hring R, Faulstich A. The permeability of the blood-CSF barrier in hydrocephalus, polyradiculitis, and meningitis. J Neurol. 2004;251:355–6.
33. Abdi K, Lai C-H, Paez-Gonzalez P, Lay M, Pyun J, Kuo CT. Uncovering inherent cellular plasticity of multiciliated ependyma leading to ventricular wall transformation and hydrocephalus. Nat Commun. 2018;9:1655.
34. Roales-Buján R, Páez P, Guerra M, Rodríguez S, Vío K, Ho-Plagaro A, et al. Astrocytes acquire morphological and functional characteristics of ependymal cells following disruption of ependyma in hydrocephalus. Acta Neuropathol. 2012;124:531–46.
35. Park R, Moon UY, Park JY, Hughes LJ, Johnson RL, Cho S-H, et al. Yap is required for ependymal integrity and is suppressed in LPA-induced hydrocephalus. Nat Commun. 2016;7:10329.
36. Ahn JH, Cho H, Kim J-H, Kim SH, Ham J-S, Park I, et al. Meningeal lymphatic vessels at the skull base drain cerebrospinal fluid. Nature. 2019;572:62–6.
37. Okuda KS, Astin JW, Misa JP, Flores MV, Crosier KE, Crosier PS. lyve1 expression reveals novel lymphatic vessels and new mechanisms for lymphatic vessel development in zebrafish. Development. 2012;139:2381–91.
38. Cui J, Xu H, Lehtinen MK. Macrophages on the margin: choroid plexus immune responses. Trends Neurosci. 2021;44:864–75.
39. Dani N, Herbst RH, McCabe C, Green GS, Kaiser K, Head JP, et al. A cellular and Spatial map of the choroid plexus across brain ventricles and ages. Cell. 2021;184:3056–e307421.
40. Taranov A, Bedolla A, Iwasawa E, Brown FN, Baumgartner S, Fugate EM et al. The choroid plexus maintains adult brain ventricles and subventricular zone

neuroblast pool, which facilitates poststroke neurogenesis. Proceedings of the National Academy of Sciences. 2024;121:e2400213121.
41. Deczkowska A, Baruch K, Schwartz M. Type I/II interferon balance in the regulation of brain physiology and pathology. Trends Immunol. 2016;37:181–92.
42. Ivashkiv LB. IFNγ: signalling, epigenetics and roles in immunity, metabolism, disease and cancer immunotherapy. Nat Rev Immunol. 2018;18:545–58.
43. Warre-Cornish K, Perfect L, Nagy R, Duarte RRR, Reid MJ, Raval P, et al. Interferon-γ signaling in human iPSC–derived neurons recapitulates neurodevelopmental disorder phenotypes. Sci Adv. 2020;6:1–17.
44. Saraswat D, Welliver RR, Ravichandar R, Tripathi A, Broome J, Hurley E, et al. Heparanome-mediated rescue of oligodendrocyte progenitor quiescence following inflammatory demyelination. J Neurosci. 2021;41:2245–63.
45. Tadokoro T, Wang Y, Barak LS, Bai Y, Randell SH, Hogan BLM. IL-6/STAT3 promotes regeneration of airway ciliated cells from basal stem cells. Proc Natl Acad Sci U S A. 2014;111:3641–9.
46. Regis G, Pensa S, Boselli D, Novelli F, Poli V. Ups and downs: the STAT1:STAT3 Seesaw of interferon and gp130 receptor signalling. Semin Cell Dev Biol. 2008;19:351–9.
47. Butturini E, de Prati AC, Mariotto S. Redox regulation of STAT1 and STAT3 signaling. Int J Mol Sci. 2020;21:1–18.
48. Salehi Z, Mashayekhi F. The role of cerebrospinal fluid on neural cell survival in the developing chick cerebral cortex: an in vivo study. Eur J Neurol. 2006;13:760–4.
49. Shinoda M, Hidaka M, Lindqvist E, Söderström S, Matsumae M, Oi S, et al. NGF, NT-3 and Trk C mRNAs, but not TrkA mRNA, are upregulated in the paraventricular structures in experimental hydrocephalus. Child's Nerv Syst. 2001;17:704–12.
50. Hochhaus F, Koehne P, Schäper C, Butenandt O, Felderhoff-Mueser U, Ring-Mrozik E, et al. Elevated nerve growth factor and neurotrophin-3 levels in cerebrospinal fluid of children with hydrocephalus. BMC Pediatr. 2001;1:2.
51. Di Curzio DL, Mao X, Baker A, Del Bigio MR. Nimodipine treatment does not benefit juvenile ferrets with kaolin-induced hydrocephalus. Fluids Barriers CNS. 2018;15:14.
52. Ballabh P, de Vries LS. White matter injury in infants with intraventricular haemorrhage: mechanisms and therapies. Nat Rev Neurol. 2021;17:199–214.
53. Krishna S, Cheng B, Sharma DR, Yadav S, Stempinski ES, Mamtani S et al. PPAR-γ activation enhances myelination and neurological recovery in premature rabbits with intraventricular hemorrhage. Proc Natl Acad Sci U S A. 2021;118.
54. Rodríguez EM, Guerra MM, Vío K, González C, Ortloff A, Bátiz LF, et al. A cell junction pathology of neural stem cells leads to abnormal neurogenesis and hydrocephalus. Biol Res. 2012;45:231–41.
55. Duy PQ, Rakic P, Alper SL, Robert SM, Kundishora AJ, Butler WE, et al. A neural stem cell paradigm of pediatric hydrocephalus. Cereb Cortex. 2023;33:4262–79.
56. Jin SC, Dong W, Kundishora AJ, Panchagnula S, Moreno-De-Luca A, Furey CG, et al. Exome sequencing implicates genetic disruption of prenatal neuro-gliogenesis in sporadic congenital hydrocephalus. Nat Med. 2020;26:1754–65.
57. Duy PQ, Weise SC, Marini C, Li XJ, Liang D, Dahl PJ, et al. Impaired neurogenesis alters brain biomechanics in a neuroprogenitor-based genetic subtype of congenital hydrocephalus. Nat Neurosci. 2022;25:458–73.
58. De Waele J, Verhezen T, van der Heijden S, Berneman ZN, Peeters M, Lardon F, et al. A systematic review on poly(I:C) and poly-ICLC in glioblastoma: adjuvants coordinating the unlocking of immunotherapy. J Exp Clin Cancer Res. 2021;40:213.
59. Okuma N, Ito M-A, Shimizu T, Hasegawa A, Ohmori S, Yoshida K, et al. Amplification of poly(I:C)-induced interleukin-6 production in human bronchial epithelial cells by priming with interferon-γ. Sci Rep. 2023;13:21067.
60. Kang S, Kishimoto T. Interplay between interleukin-6 signaling and the vascular endothelium in cytokine storms. Exp Mol Med. 2021;53:1116–23.
61. McLoughlin RM, Witowski J, Robson RL, Wilkinson TS, Hurst SM, Williams AS, et al. Interplay between IFN-gamma and IL-6 signaling governs neutrophil trafficking and apoptosis during acute inflammation. J Clin Invest. 2003;112:598–607.
62. Bluyssen HAR, Rastmanesh MM, Tilburgs C, Jie K, Wesseling S, Goumans M-J, et al. IFN gamma-dependent SOCS3 expression inhibits IL-6-induced STAT3 phosphorylation and differentially affects IL-6 mediated transcriptional responses in endothelial cells. Am J Physiol Cell Physiol. 2010;299:C354–62.
63. Kataru RP, Kim H, Jang C, Choi DK, Koh BI, Kim M, et al. T lymphocytes negatively regulate lymph node lymphatic vessel formation. Immunity. 2011;34:96–107.
64. Cromer WE, Zawieja SD, Tharakan B, Childs EW, Newell MK, Zawieja DC. The effects of inflammatory cytokines on lymphatic endothelial barrier function. Angiogenesis. 2014;17:395–406.
65. Garnier L, Pick R, Montorfani J, Sun M, Brighouse D, Liaudet N, et al. IFN-γ-dependent tumor-antigen cross-presentation by lymphatic endothelial cells promotes their killing by T cells and inhibits metastasis. Sci Adv. 2022;8:eabl5162.
66. Zhu L, Bai Y, Li A, Wan J, Sun M, Lou X, et al. IFN-γ-responsiveness of lymphatic endothelial cells inhibits melanoma lymphatic dissemination via AMPK-mediated metabolic control. Biochim Biophys Acta Mol Basis Dis. 2024;1870:167314.
67. Pourabdolhossein F, Gil-Perotín S, Garcia-Belda P, Dauphin A, Mozafari S, Tepavcevic V, et al. Inflammatory demyelination induces ependymal modifications concomitant to activation of adult (SVZ) stem cell proliferation. Glia. 2017;65:756–72.
68. Fernández-Arjona M, del León-Rodríguez M, López-Ávalos A, Grondona MD. Microglia activated by microbial neuraminidase contributes to ependymal cell death. Fluids Barriers CNS. 2021;18:1–14.
69. Granados-Durán P, López-Ávalos MD, Hughes TR, Johnson K, Morgan BP, Tamburini PP, et al. Complement system activation contributes to the ependymal damage induced by microbial neuraminidase. J Neuroinflammation. 2016;13:1–15.

Publisher's note